



**HAL**  
open science

# Harmonic propagation of variability in surface energy balance within a coupled soil-vegetation-atmosphere system

P. Gentine, J. Polcher, D. Entekhabi

► **To cite this version:**

P. Gentine, J. Polcher, D. Entekhabi. Harmonic propagation of variability in surface energy balance within a coupled soil-vegetation-atmosphere system. *Water Resources Research*, 2011, 47 (5), pp.W05525. 10.1029/2010WR009268 . hal-01119189

**HAL Id: hal-01119189**

**<https://hal.science/hal-01119189>**

Submitted on 22 Feb 2015

**HAL** is a multi-disciplinary open access archive for the deposit and dissemination of scientific research documents, whether they are published or not. The documents may come from teaching and research institutions in France or abroad, or from public or private research centers.

L'archive ouverte pluridisciplinaire **HAL**, est destinée au dépôt et à la diffusion de documents scientifiques de niveau recherche, publiés ou non, émanant des établissements d'enseignement et de recherche français ou étrangers, des laboratoires publics ou privés.

# Harmonic propagation of variability in surface energy balance within a coupled soil-vegetation-atmosphere system

P. Gentine,<sup>1</sup> J. Polcher,<sup>2</sup> and D. Entekhabi<sup>3</sup>

Received 7 March 2010; revised 7 February 2011; accepted 23 February 2011; published 19 May 2011.

[1] The response of a soil-vegetation-atmosphere continuum model to incoming radiation forcing is investigated in order to gain insights into the coupling of soil and atmospheric boundary layer (ABL) states and fluxes. The response is characterized through amplitude and phase propagation of the harmonics in order to differentiate between the response of the system to forcing at different frequencies (daily to hourly to near instantaneous). Stochastic noise is added to the surface energy balance. The amplitude of the noise is maximum at midday when the incoming radiative forcing is also at its peak. The temperatures and turbulent heat fluxes are shown to act as low-pass filters of the incoming radiation or energy budget noise variability at the surface. Conversely, soil heat flux is shown to act as a high-pass filter because of the strong contrast in the soil and air heat capacities and thermal conductivities. As a consequence, heat diffusion formulations that numerically dampen such forcing are potentially incapable of representing rapid fluctuations in soil heat flux ( $\leq 30$  min) and therefore introduce errors in the land-surface energy partitioning. The soil-vegetation-ABL continuum model and an electrical analogy for it are used to explain the frequency-dependent differences in the relative effectiveness of turbulent heat fluxes versus ground heat flux in dissipating noise in radiative forcing.

**Citation:** Gentine, P., J. Polcher, and D. Entekhabi (2011), Harmonic propagation of variability in surface energy balance within a coupled soil-vegetation-atmosphere system, *Water Resour. Res.*, 47, W05525, doi:10.1029/2010WR009268.

## 1. Introduction

[2] The daily cycle of incoming radiative forcing at the land surface results in changes in the surface energy balance through the modification of outgoing radiative, turbulent, and soil heat fluxes. These adjustments impact the profiles of moisture, temperature, and heat fluxes along the whole soil-vegetation-atmosphere continuum. The induced changes in the temperature profiles affect the components of the land-surface energy budget, leading to feedback mechanisms and a modified coupling between the soil, vegetation, and atmospheric boundary layer (ABL). This coupling can in turn modulate the temporal response of the land-surface, soil, and ABL systems, with important repercussions for the accuracy of their prediction and estimation.

[3] Accurate estimation of the components of the land-surface energy budget is required to improve weather and hydrological forecasts. A quantitative understanding of the feedbacks and coupling within the soil-vegetation-atmosphere continuum is central for these improvements. However, measurements and modeling of the daily land-surface heat fluxes are inherently prone to errors because of sensor, modeling, or sampling errors. These errors lead to

erroneous surface energy balance estimation, with possible biases in one or several of its components. Evaluation of the repercussion of these errors in the soil-vegetation-atmosphere continuum is fundamental to assessing their impacts on the prediction and variability of the soil and ABL systems. The study by *Deardorff* [1978] is an example of one of the earlier studies on the influence of land-surface energy budget errors on the soil-ABL system. Other numerical studies of soil-vegetation-ABL continuum modeling and sensitivity analysis include *Santanello et al.* [2005, 2007] and *Huang and Margulis* [2010]. Studies such as those by *Callies et al.* [1998] and *Hess* [2001] attempt to work in the reverse direction and estimate the determinant factors of the surface energy balance from the fluctuations and temporal patterns in the soil and ABL states. Regardless of whether the focus is on the fidelity of estimating the soil and ABL states or on inferring the surface energy balance components from soil and ABL measurements, the feedbacks in the soil-vegetation-atmosphere continuum are key to making linkages between the states and fluxes in the system. This study is focused on understanding these linkages, and it specifically focuses on the harmonic response in terms of gain and phase spectra that indicate the strength of coupling and lag-lead relationships at different temporal scales.

[4] Incoming radiation forcing is predominantly daily periodic, leading to a similar strong periodicity within the soil-ABL system. The phase and amplitude of the state and flux responses are key to the understanding of the feedback mechanisms and land-atmosphere coupling. Most studies of land-atmosphere interactions have been performed with

<sup>1</sup>Department of Applied Physics and Applied Mathematics, Columbia University, New York, New York, USA.

<sup>2</sup>Laboratoire de Météorologie Dynamique du CNRS, Paris, France.

<sup>3</sup>Ralph M. Parsons Laboratory, Massachusetts Institute of Technology, Cambridge, Massachusetts, USA.

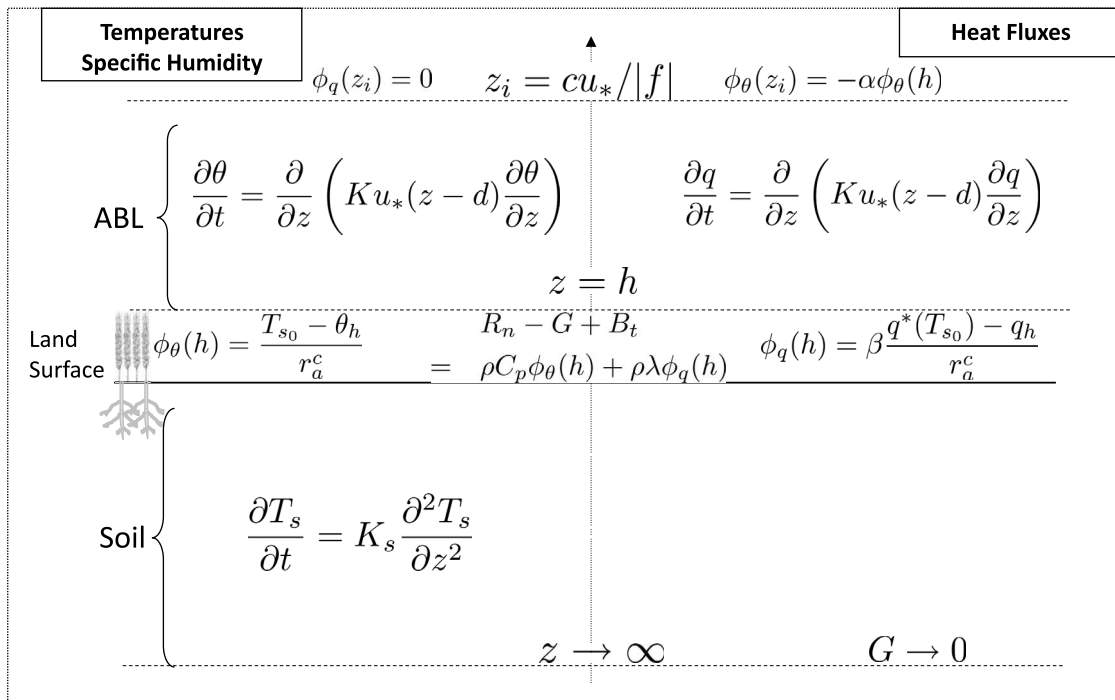


**Figure 1.** Schematic of the soil-vegetation-ABL continuum model with the governing equations in each domain. The coupling occurs at the surface with  $\phi_\theta = \overline{w'\theta'} = H/\rho C_p$  and  $\phi_q = \overline{w'q'} = \lambda E/\rho\lambda$ .

numerical models that can capture the nonlinearities of the coupled system. Such approaches are valuable in that they include as much of the full complexity of the system as is known. Simpler models [e.g., see Lettau, 1951; Manqian and Jinjun, 1993; Kimura and Shimizu, 1994; Brubaker and Entekhabi, 1995; Kim and Entekhabi, 1998; Zeng and Neelin, 1999; Wang and Mysak, 2000; Margulis and Entekhabi, 2001; Van de Wiel et al., 2003; Baudena et al., 2008; Gentine et al., 2010] that can yield analytic solutions have their own value. They may not include all the known complex detail, but if they capture the first-order effects, their compact solution can be used to gain important physical insights.

[5] In the present study we use an extended version of the analytical linear model of the soil-vegetation-ABL continuum introduced by Gentine et al. [2010] in order to analyze the phase and amplitude responses at different temporal frequencies. Spectral representation of the state of the soil-vegetation-atmosphere continuum requires linear models that capture the essential physics and linkages since they can be solved using (temporal) Fourier decomposition. The states and fluxes in the soil-vegetation-atmosphere continuum are decomposed into harmonics, unveiling their phase and amplitude response to diurnal radiative forcing at each harmonic. Essentially, the soil and atmosphere states are conceptualized as linear filters of the radiative forcing. A characterization of these filters in quantitative gain and phase spectra are the principal original contributions of the first part of this study. In the second part, the repercussion of temporal variability in the land-surface energy budget is investigated using an injected noise whose strength follows the daily radiative forcing at the land surface. The time-continuous noise at the land surface is developed in terms of harmonics, revealing interesting and insightful

features of noise propagation within the soil-vegetation-ABL continuum.

## 2. Method

### 2.1. Linearized Land-Atmosphere Model

[6] A schematic representation of the soil-vegetation-atmosphere model is shown in Figure 1. It represents the soil-vegetation-ABL continuum as a set of partial differential equations, which are coupled at their respective boundaries. In the soil, the thermal heat diffusion based on energy conservation and gradient-driven heat flux with constant coefficients governs the soil temperature profile evolution. In the ABL a linearly increasing thermal diffusivity (with height) and heat conservation govern the system. Air specific humidity in the ABL is a passive scalar. The height of the boundary layer is fixed as a function of model parameters, but the effects of entrainment are included (see section 2.2). The soil and ABL are coupled through a shallow vegetation layer that allows a discontinuity in the temperature across the soil-ABL boundary. The vegetation layer is assumed to be relatively shallow and to have negligible heat capacity compared to the soil medium.

[7] Those assumptions are similar to most current operational state-of-the-art land-surface models using either single or dual source formulation for energy balance in presence of vegetation (e.g., in the Common Land Model) (Y. Dai et al., Common Land Model (CLM): Technical documentation and user's guide, 2001). The transfers of heat from the surface to the atmosphere are governed by aerodynamic resistances. Latent heat flux is additionally affected by stomatal resistances. In this study the well-known “big-leaf” approach is adopted, which is also commonly used in many operational models (e.g., the Interactions Soil

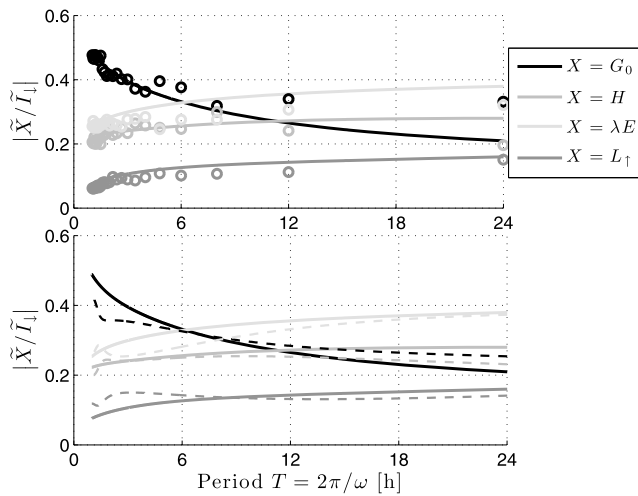


**Figure 2.** Comparison between the harmonics of surface heat fluxes:  $G_0$ , soil;  $H$ , sensible; and  $\lambda E$ , latent heat flux and outgoing radiation from the theoretical model (solid lines) with 66 days of continuous observations, as a function of the period  $T = 2\pi/\omega$ . (top) The comparison with mean observed spectrum averaged across days (i.e., the power spectrum of each flux is averaged at each daily frequency across all measurement days). The high frequencies are well captured by the theoretical model. (bottom) The comparison with the Yule-Walker filter of the data (dashed lines), which is more representative of the lower-frequency component by construct. This lower-frequency component is well reproduced by the theoretical model.

Biosphere Atmosphere scheme) [Noilhan and Mahfouf, 1996]. Evaporation at the land surface is a function of atmospheric evaporative demand, energy balance, and a surface (soil and vegetation) resistance factor. Plant physiology and associated stomatal resistance does change as a function of environmental conditions such as air temperature, air humidity, and insulation. These complex dependencies vary with plant species. For the purposes of this study the big-leaf approach is adequate and captures the principal control of surface water availability on latent heat flux. We perform sensitivity to the evaporation reduction function parameter in order to assess the impact of the simplification.

[8] Another issue that distinguishes the big-leaf approach from others is the impact of shading by vegetation. More complicated models of vegetation canopy allow fractional shading of the surface that reduces the ground heat flux. This issue is particularly important when the vegetation coverage is dense. In the nominal situation of this study and the conditions of the field measurements evaluation of the model by Gentine *et al.* [2010], the surface below the frequently irrigated wheat crop was characterized by significant ground heat flux. Heat flux reached a peak of  $200 \text{ W m}^{-2}$  even when the Leaf Area Index reached past 3. Under these conditions, the big-leaf approach, which treats the land surface as a mixture of soil and vegetation, is applicable. Nonetheless, in the presence of tall and dense vegetation, for example, forests, our approach needs to be reevaluated. For dense vegetation cover the dual-source approach may be more appropriate. The dual-source approach would allow the decoupling between the soil and canopy temperatures that in turn lead to a further reduction of the surface soil heat

flux. The inclusion of heat storage within the vegetation layer could modify the spectral response of the fluxes. The effect of the vegetation characteristics on the surface heat flux spectra requires further and more thorough investigation.

[9] The model used in the present study is based on the model introduced by Gentine *et al.* [2010], originally inspired by the work of Lettau [1951]. Eight parameters characterize the system: friction velocity  $u_*$ , canopy aerodynamic resistance  $r_a^c$ , water availability  $\beta$  (evaporative control), soil thermal diffusivity  $K_s$ , soil heat capacity  $C_s$ , vegetation height  $h$ , surface albedo  $\alpha_s$ , and emissivity  $\epsilon_s$  (see notation section for a list of variables and symbols). Vegetation height, albedo, and emissivity were obtained directly from observations. The other parameters are manually calibrated using observations of infrared surface temperature, screen-level temperature, and sensible and latent heat fluxes. In section 5 sensitivity to these parameters are quantitatively evaluated, and their impacts on the conclusions are discussed. The model is shown to capture the first-order features of the coupled system and to accurately replicate the daily course of observed heat fluxes and temperatures both at the land surface and at screen level [see Gentine *et al.*, 2010] in comparison with measurements from the SudMed project [see Duchemin *et al.*, 2006; Gentine *et al.*, 2007; Chehbouni *et al.*, 2008]. The model is able to capture the diurnal cycle of the state variables and fluxes near the surface well. The calibrated friction velocity was in almost perfect agreement with the mean daily observed friction velocity.

[10] Gentine *et al.* [2010, Figure 5] show that the calibrated model captures the essential features contained in the mean diurnal cycle (amplitude and phase) of the surface components of the surface energy balance. The phase differences and amplitudes of the surface energy balance components of the model are consistent with the observations given similar incident radiative forcing. In order to compare the variability, especially high-frequency variability, inherent in the model with those observed in the field, spectral analysis of the surface energy balance components is performed. Figure 2 shows the comparison of the theoretical model spectrum of surface energy balance components (solid line) with the SudMed field observations (circles). Observations for 66 days of the field experiment that have no gaps and allow Fourier analysis are used. The observed spectra of the surface fluxes are well reproduced even though a single representative value for all parameters are used in the model and the field observations have synoptic weather and irrigation perturbations. But these perturbations mostly affect the spectrum at frequencies about the diurnal period. In particular soil heat flux is responding more vigorously to high daily frequencies (acts as a high-pass filter), whereas other flux terms tend to pass mostly the lower daily harmonics in the radiative forcing. Land-surface temperature is also a low-pass filter of incident radiation. The model is thus reasonably able to characterize the emergent behavior of the coupled land-atmosphere system at the surface in terms of both mean behavior as well as variability.

[11] The model relies on important simplifying assumptions in order to derive an analytical solution in the form of temporal harmonics as a Fourier series. The reader is referred to Gentine *et al.* [2010] for a complete list of the hypotheses underlying the model structure. The most important assumptions are: (1) the atmosphere is in a near-

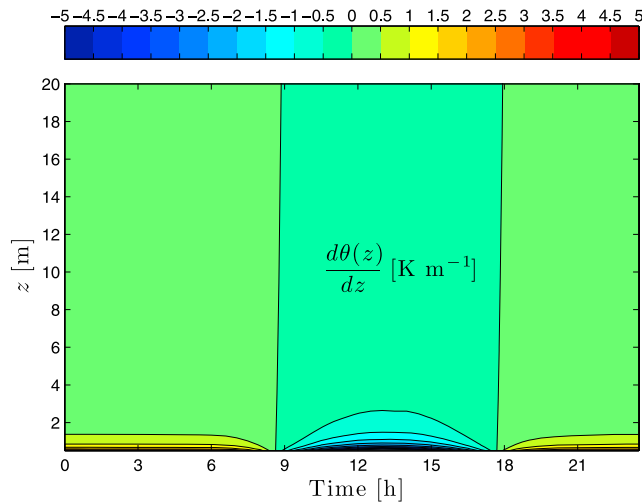


**Figure 3.** Gradient of potential temperature in the lower surface layer (20 m) as a function of hour of day.

neutral to unstable turbulent state, (2) friction velocity is assumed to be constant throughout the day, (3) the ABL height is fixed and related to system parameters, and (4) the evaporation reduction (water availability) factor  $\beta$  is constant throughout the day. Even though those assumptions are drastic, they still allow for a good representation of the surface air layer (within the first tens of meters), which is our subregion of interest within the ABL.

[12] As discussed earlier, one especially important point is that the model is able to capture the essential physics of the surface energy partitioning and thus the emergent behavior of the coupled system under very diverse environmental and soil moisture conditions. The first major assumption is that the atmosphere is in a near-neutral to unstable turbulent state. The main focus of this study and use of the model are to analyze the temporal spectra of turbulent fluxes and states at the surface boundary with the atmosphere. The surface air layer that is confined to the first few meters to tens of meters above the surface is thus the most influential section of the atmospheric boundary layer. Restricted focus on this layer is more compatible with the assumption on the turbulent state of the atmosphere. Figure 3 shows the vertical gradient in temperature in the top 20 m of the atmosphere as a function of hour of day. There is a discontinuity at the surface in the construct of the model (see Figure 1 and treatment of vegetation canopy), which is further confirmed by this contour map. Figure 3 shows that during daytime, which is the period of concern in this study, the assumption of near-neutral to unstable turbulent condition is evident in the model response to incoming radiation forcing.

[13] The second major assumption is a fixed value for friction velocity during a typical fair-weather day. The quality of this assumption is discussed in detail in section 5. The most stringent assumption is certainly the third, that holds a fixed boundary-layer height. This assumption, however, cannot be relaxed and still allow an analytical solution. There are less repercussions from this assumption if we consider only the lower part of the surface layer, constrained by the logarithmic profile induced by solar heating at the surface. In fact *Lettau* [1951] introduced the

coupled model as a coupled land-surface layer model and did not consider the whole boundary layer. In particular, the model is still able to capture well the course of screen-level temperature [*Gentine et al.*, 2010].

[14] The advantage and novelty of this linearized model is that it resolves the soil and ABL profiles of scalars and heat fluxes in the temporal Fourier domain. This characteristic allows the quantitative evaluation of the amplitude and phase propagation of incoming radiation in the soil-vegetation-atmosphere continuum as a continuous function of height and depth and, more importantly, continuous in time at all subdiurnal frequencies. All variables are written as Fourier series responding to radiative forcing:

$$X(t, z) = \langle X(z) \rangle + \sum_{n=-N_{\text{FFT}}, n \neq 0}^{N_{\text{FFT}}} \widetilde{X}_n(z) \exp(j\omega_n t), \quad (1)$$

where  $\omega_n = 2n\pi/T_{\text{day}}$  is the harmonic angular frequency. In addition the temporal resolution of the model only depends on that of the input through the Nyquist frequency. However, because of the linearity of the model, the response (output over input in the frequency domain) can be calculated above the Nyquist frequency at all daily harmonics. Consequently, insights into the land-atmosphere system can be made at higher daily frequencies than the ones observed. The model outputs are continuous in both time and space (height and depth), thus allowing investigations at smaller scales than those allowed by most numerical models.

[15] The amplitude and phase of the harmonics of this model state can be readily studied as a function of the model parameters and forcing. The different components of the soil-surface-ABL continuum are linear filters of the radiative forcing at the land surface. Finally, since the daily radiative forcing is assumed to be periodic (dominated by the diurnal cycle), the model study does not require the specification of initial profiles. This is highly advantageous for a sensitivity study when compared to more complex numerical models. In particular, the statistics of the variables within the system can be estimated without residual correlation with initial conditions that often hampers numerical studies.

## 2.2. Deterministic Incoming Radiation Forcing

[16] In the work by *Gentine et al.* [2010], the model is forced by periodic net radiation at the land surface. Here we instead use the incoming radiation at the surface  $I_{\downarrow}$ , defined as the sum of net solar  $S_{\downarrow}$  and incoming thermal components  $L_{\downarrow}$  as  $I_{\downarrow} = (1 - \alpha_s)S_{\downarrow} + L_{\downarrow}$ . The net radiation forcing is linearized around the mean daily land-surface temperature in order to use  $I_{\downarrow}$  as the forcing:

$$R_n(t) = \underbrace{(1 - \alpha_s)\bar{S} + \bar{L}_{\downarrow} - \varepsilon_s \Sigma \bar{T}_{s_0}^4}_{\bar{R}_n} + \underbrace{(1 - \alpha_s)\Delta S_{\downarrow}(t) + \Delta L_{\downarrow}(t) - 4\varepsilon_s \Sigma \bar{T}_{s_0}^3 \Delta T_{s_0}(t)}_{\Delta R_n(t)}. \quad (2)$$

$\bar{X}$  represents the mean daily value of  $X$ , and  $\Delta X(t)$  represents the temporal variations of  $X$  around its mean.

[17] Compared to *Gentine et al.* [2010], the linear model is modified in several ways.

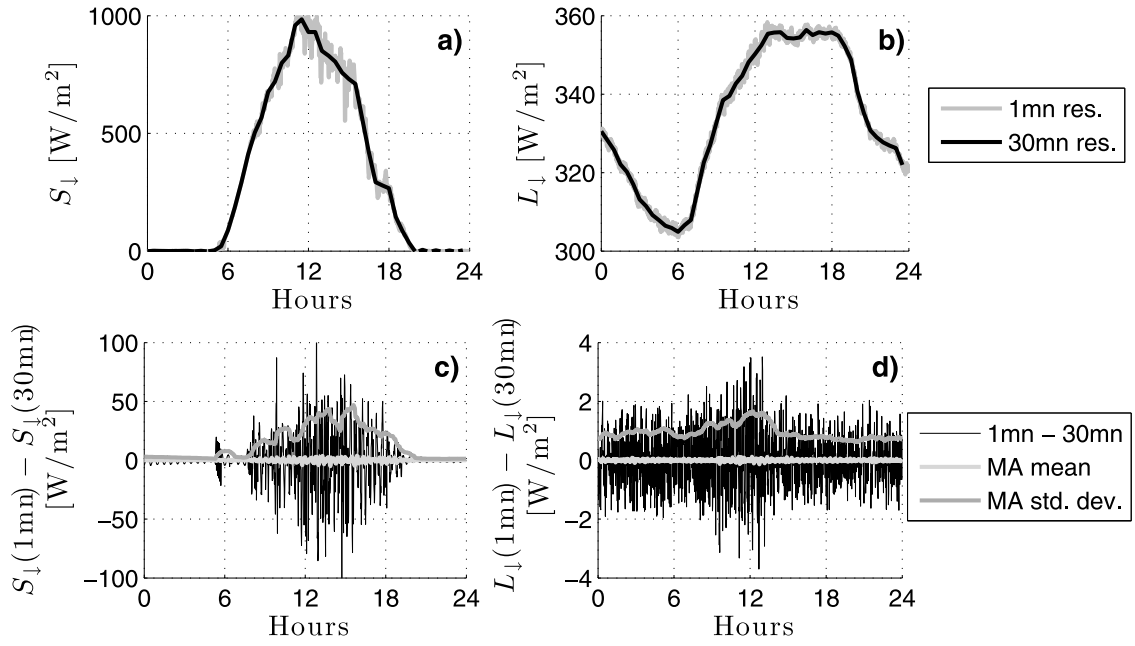


**Figure 4.** (a) Shortwave and (b) longwave downward radiation, at a 1 min and 30 min resolution, measured during 6 June 1997 over the Southern Great Plain experiment in Lamont, Oklahoma. (c) Shortwave and (d) longwave downward radiation residual between 1 min and 30 min resolution measurements, along with 30 min moving average (MA) mean (light gray) and 30 min MA standard deviation (dark gray).

[18] 1. Latent heat flux at the land surface is expressed using a bulk formulation [Deardorff, 1978]:

$$\lambda E_h = \frac{\rho \lambda \beta}{r_a^c} [q^*(T_{s_0}) - q_h]. \quad (3)$$

The parameter  $\beta$  reduces the evaporation below its limiting potential value corresponding to a moist surface. This parameter is related to soil moisture in the root zone, and it is assumed to be constant throughout the day. The main difficulty of the latent heat flux is that the saturated specific humidity is a nonlinear function of temperature. To the first-order approximation, this equation can be linearized around the mean daily land-surface temperature:

$$q^*(T_{s_0}) = q^*(\bar{T}_{s_0}) + \gamma_{\bar{T}_{s_0}} (T_{s_0} - \bar{T}_{s_0}). \quad (4)$$

Introduction of dynamic latent heat flux term in the surface energy balance necessitates inclusion of a specific humidity variable in the ABL.

[19] 2. A diffusion equation governing the evolution of specific humidity in the ABL is added, and it is similar to the diffusion equation for potential temperature presented by Gentine et al. [2010]. This equation has a Neuman boundary condition on top of the ABL and a jump condition at vegetation height  $h$ .

[20] 3. Entrainment is added on top of the ABL through a parameter  $\alpha$  such that  $H(z_i) = -\alpha H_h$ , in order to account for the entrainment of warmer air into the ABL from the free troposphere.

[21] In this study we focus on the lower part of the surface layer that extends from the top of the vegetation canopy to less than 10 m above the land surface. This lower part of the surface layer contains important ABL dynamics that are

relevant for surface energy balance coupling to the ABL. Our focus on this surface layer region is more consistent with our assumptions about fixed ABL height and near-neutral stability. In fact, Lettau [1951] introduced the atmospheric model as a representation of the surface layer alone. The focus on the surface layer is prudent since at higher elevations in the ABL the time varying ABL has significant influence on the dynamics of temperatures and fluxes. It is also important to note that we principally focus on the daytime hours so that the effects of nighttime ABL stable stratification do not adversely impact our conclusions.

### 2.3. Variability in the Land-Surface Energy Budget: Brownian Bridge Forcing

[22] In the second part or stochastic extension of this study, the energy closure at the surface is assumed to contain variability in the form of an additive noise. This noise is introduced to represent the daily course of energy budget random variability at the land surface, be they due to measurements and modeling inaccuracies or rapid variations of incoming radiation (e.g., through intermittent passage of clouds). The noise or error in the energy budget is introduced in the form of a Brownian bridge  $B_{T_{\text{day}}}(t)$ . This noise is added to the energy budget at the land surface to simulate the diurnal course of the variability in the energy budget. The linearized energy budget at the land surface is

$$\underbrace{I_{\downarrow}(t) - \epsilon_s \Sigma T_s(0, t)^4 - G(0, t)}_{R_n(t)} + B_{T_{\text{day}}}(t) = \underbrace{H(h, t)}_{\rho C_p \phi_q(h, t)} + \underbrace{\lambda E(h, t)}_{\rho \lambda \phi_q(h, t)}. \quad (5)$$

[23] Figure 4 displays the typical fair-weather diurnal course of shortwave and longwave radiation at the land

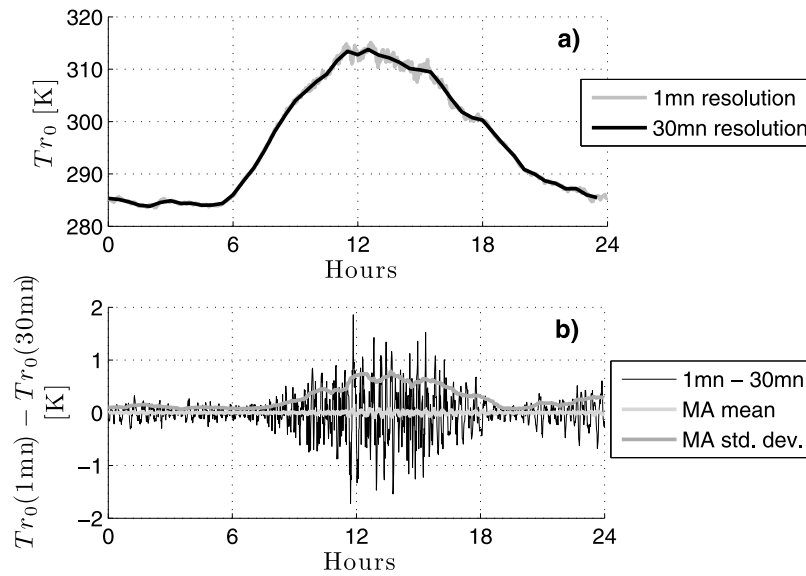


**Figure 5.** (a) Infrared surface temperature, at a 1 min and 30 min resolution, measured during 6 June 1997 over the Southern Great Plain experiment in Lamont, Oklahoma. (b) Infrared surface temperature residual between 1 min and 30 min resolution measurements, along with 30 min moving average (MA) mean (light gray) and 30 min MA standard deviation (dark gray).

surface as observed on the Central Facility of the Southern Great Plains experiment on 5 June 1997, at a 1 min and 30 min temporal resolution. The coarser (30 min) resolution does not capture the spikes in the solar radiation time series, as shown in Figure 4a. The difference between solar radiation measured at a 1 min and 30 min resolution exhibits a strong diurnal cycle with a peak at solar noon, as evident in Figure 4c. The changes in longwave radiation at the two disparate temporal resolutions are negligible in this fair-weather case, as evident in Figure 4d. The high-frequency variations in the surface radiation can have significant impacts on land-surface energy partitioning. They especially influence land-surface temperature, as observed in the infrared temperature time series (Figure 5). Typical deviations of about 1 K are observed in response to rapid solar radiation variations of about  $100 \text{ W m}^{-2}$ . The variance of the noise in incoming radiation (below 30 min) exhibits a parabolic curve with a maximum at around solar noon and negligible value late at night (Figure 4c). This shape of the noise time series motivates the use of a Brownian bridge (BB) for noise modeling [Deheuvels, 2007]. Its variance is parabolic, with zero value at midnight and a maximum at noon, as shown in Figure 6. The Brownian bridge can also capture variability on timescales smaller than 30 min that fits the daily cycle of radiation.

[24] The BB is a continuous stochastic process whose probability distribution is the conditional distribution of the Brownian motion with  $B_{T_{\text{day}}}(0) = B_{T_{\text{day}}}(T_{\text{day}}) = 0$ . The BB noise intensity, as represented by the dependence of its standard deviation on hour of day (Figure 6), has a distinct diurnal cycle. This is a deliberate choice to preserve the diurnal course of the surface energy balance variability.

[25] The Brownian bridge is unbiased so that the energy budget is closed on average over all realizations of the random walk. This average could represent different model runs or different sensor measurements, that is, different

realizations of the process as depicted in Figure 6. A bias could be added, but on the basis of examples in Figure 4c, we take it to be unbiased.

#### 2.4. Brownian Bridge Properties

[26] In this section the key properties of the BB are described. In particular, we focus on the Fourier transform of the process, since it serves as the foundation for the rest of the study. The BB is rewritten as a modified Brownian motion:

$$\sigma \widehat{B}_{T_{\text{day}}}(t) = \sigma \left\{ \widehat{W}_{T_{\text{day}}} - \frac{t}{T_{\text{day}}} \widehat{W}_{T_{\text{day}}} \right\}, \quad (6)$$

where  $\widehat{B}_{T_{\text{day}}}(t)$  is the normalized BB.  $\widehat{W}_{T_{\text{day}}}$  is the normalized Brownian motion, and  $\sigma$  is the volatility of the process. The covariance function of the BB is given by

$$\text{cov}(\sigma \widehat{B}_{T_{\text{day}}}(s), \sigma \widehat{B}_{T_{\text{day}}}(t)) = \sigma^2 \left( \min(s, t) - \frac{st}{T} \right). \quad (7)$$

The variance of the process is  $\sigma^2 \left( t - \frac{t^2}{T_{\text{day}}} \right)$ , which is null at midnight (i.e.,  $t = 0$  or  $T_{\text{day}}$ ) and is maximum at noon ( $T_{\text{day}}/2$ ) and equal to  $\sigma^2 T_{\text{day}}/4$ . The population standard deviation is displayed in Figure 6.

[27] The BB has a natural Fourier decomposition:

$$\begin{aligned} B_{T_{\text{day}}} &= \sum_{k=-\infty}^{+\infty} \widetilde{B}_k \exp(j\omega_k t) \\ &= \langle B_0 \rangle + \sum_{k=1}^{+\infty} \left( \widetilde{B}_k \exp(j\omega_k t) + \widetilde{B}_k^* \exp(-j\omega_k t) \right), \end{aligned} \quad (8)$$

with  $\widetilde{B}_k$ ,  $k \neq 0$  being (pairwise) independent complex Gaussian random variables distributed as  $N(0; \sigma^2 T_{\text{day}}/4n^2\pi^2)$  and  $\langle B_0 \rangle$  being a real Gaussian random variable distributed as  $N(0; \sigma^2 T_{\text{day}}/12)$ .

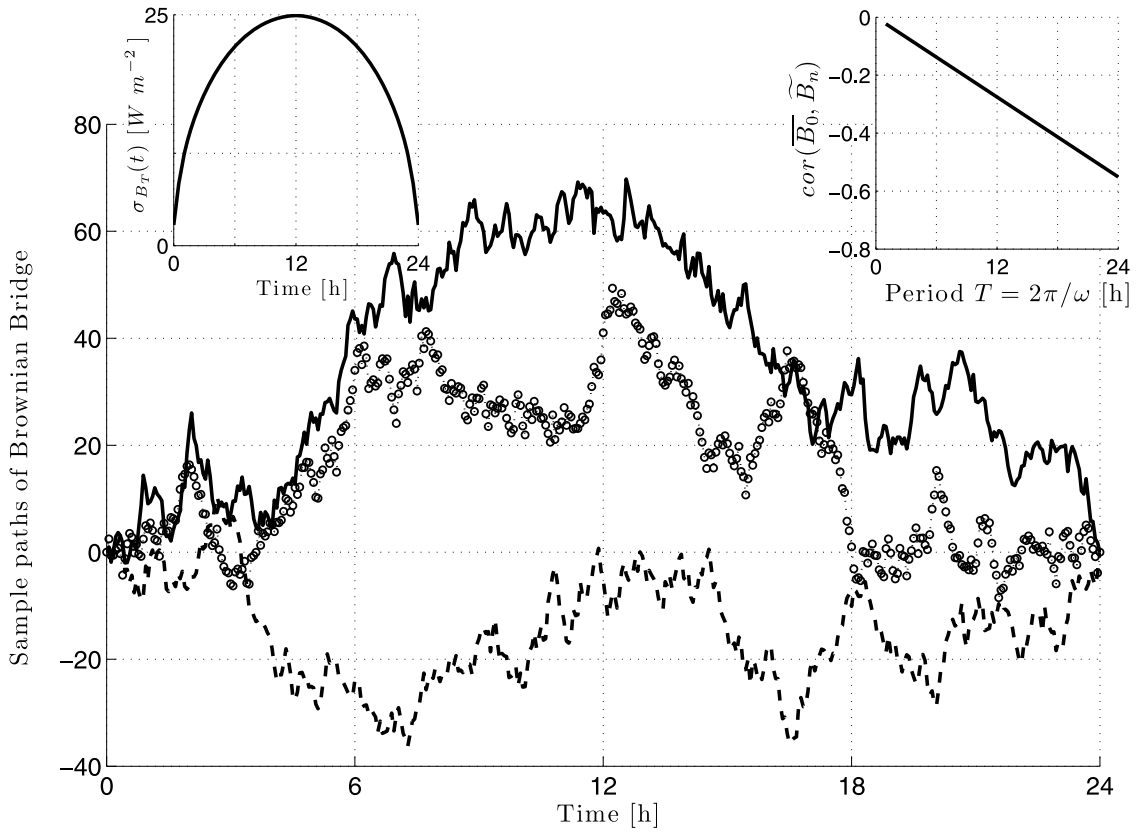


**Figure 6.** Sample paths of the Brownian bridge as a function of time. Left inset shows standard deviation as a function of time; right inset shows the correlation between the harmonics and the steady state component of the Brownian bridge as a function of the period  $T$ .

[28] Since the Fourier coefficients are Gaussian random variables, their pairwise covariances are sufficient to determine higher moments and distributional features. These covariances are

$$\forall n \geq 1: \quad \text{var } \widetilde{B}_n = \mathbb{E} \widetilde{B}_n \widetilde{B}_n^* = \frac{\sigma^2 T_{\text{day}}}{4n^2 \pi^2}, \quad (9)$$

$\forall (n_1, n_2): n_1 \neq 0 \neq n_2, n_1 \neq n_2:$

$$\text{cov}(\widetilde{B}_{n_1}, \widetilde{B}_{n_2}) = \mathbb{E}(\widetilde{B}_{n_1} \widetilde{B}_{n_2}^*) = 0 = \mathbb{E}(\widetilde{B}_{n_1} \widetilde{B}_{n_2}) = \text{cov}(\widetilde{B}_{n_1}, \widetilde{B}_{n_2}^*), \quad (10)$$

$$\text{cov}(\widetilde{B}_n, \widetilde{B}_n^*) = \mathbb{E} \widetilde{B}_n \widetilde{B}_n = 0. \quad (11)$$

Most of the noise energy (variance) is concentrated in the lowest frequencies of the spectrum,  $\omega_n n \leq 6$  or periods  $T \geq 4$  h, as seen in Figure 6. Indeed the BB, which is a conditioned Brownian motion, can be thought of as an integral of the white noise whose spectrum is flat.

[29] The correlation between the steady state Fourier coefficient  $\langle B_0 \rangle$  and the different harmonics  $\widetilde{B}_n$  is also plotted in Figure 6. Harmonics of low frequency (high period  $T$ ) are negatively correlated with the steady state coefficient, whereas high-frequency (low period  $T$ ) harmonics are almost uncorrelated and thus independent (as Gaussian random variables) of the steady state value. The

periodicity of the BB creates these correlations as the bridge is constrained to reach a null value in both 0 and  $T_{\text{day}}$ . Indeed the diurnal bias (zero harmonic) is compensated by other diurnal harmonics in order for the bridge to vanish at midnight. Lower harmonics compensate for the bias because they are more energetic (more variance).

[30] These statistics form the basis for the error forcing of the soil-ABL coupled model. They are used to express the variance and correlations of the different state variables. The statistics of the other variables within the soil-vegetation-atmosphere continuum are derived analytically as a function of the Brownian bridge harmonics.

## 2.5. Solution as a Superposition of Deterministic and Stochastic Forcing

[31] The land-atmosphere model can be thought of as the superposition of the solution of a deterministic problem, forced by the (deterministic) incoming radiation at the land surface  $I_1$  and of a stochastic problem, forced by the BB  $B_{T_{\text{day}}}$ . To fully solve the problem in the Fourier domain, the specification of the mean daily value of potential temperature and specific humidity at any height  $z_1$  are required. This is necessary for the steady state solution of the soil and atmospheric profiles. The steady state solution determines the mean daily land-surface temperature (LST) that is required for the linearization of outgoing radiation from the surface and specific humidity at saturation at the surface. *Gentine et al.* [2010] shows that the linearization of the

equations still yields reasonable results when evaluated against field measurements.

## 2.6. Stochastic Response to Surface Energy Budget Variability

[32] The solution to the stochastic part of the problem represents the ways in which variability propagates in the soil-vegetation-ABL continuum. The amplitude of the BB is small compared to the deterministic incoming radiation forcing at the land surface. Nonetheless, the propagation of variability can be discerned from the gain spectra amplitude and the phase spectra. With the noise level as a relatively small perturbation on the deterministic forcing, the linearization remains an adequate approximation of the problem. For larger values of the energy budget noise, the effects of nonlinearities could become important. Such effects have been evaluated using Monte Carlo simulations (not shown) and this transition toward nonlinear processes will be studied in further detail in a forthcoming study. In the present study the maximum standard deviation of the BB is assumed to be  $25 \text{ W m}^{-2}$ . This is relatively small when compared to the peak amplitudes of shortwave incoming radiation ( $800 \text{ W m}^{-2}$ ) and longwave incoming radiation ( $300 \text{ W m}^{-2}$ ).

### 2.6.1. Boundary Conditions

[33] All stochastic variables resulting from the BB perturbation (denoted with primes) are the result of a linearization of the equations around the mean deterministic state (denoted with an overbar) and are represented as Fourier series:

$$X'(t, z) = \langle X'(z) \rangle + \sum_{n \in \mathbb{Z}^*} \widetilde{X}'_n(z) \exp(j\omega_n t). \quad (12)$$

Because of the linearity, the perturbed variables are solutions of the same equations as the deterministic forcing, but the boundary conditions are modified as follows:

[34] 1. The incoming radiation forcing at the land surface is now replaced by the BB:  $B_{T_{\text{day}}}$ .

[35] 2. The perturbation soil heat flux vanishes at far field:  $\lim_{z \rightarrow -\infty} G'(z) = 0$ .

[36] 3. The perturbation turbulent heat fluxes are null on top of the ABL:  $\phi'_\theta(z_i) = 0$  and  $\phi'_q(z_i) = 0$ .

[37] 4. The perturbation sensible heat flux at the land surface is given by

$$\phi'_\theta(h) = \frac{T'_{s_0} - \theta'_h}{r_a^c}. \quad (13)$$

[38] 5. The perturbation latent heat flux at the land-surface boundary is linearized as

$$\phi'_q(h) = \frac{\beta}{r_a^c} \{ \gamma_{T_{\text{deep}}} T'_{s_0} - q'(h) \}, \quad (14)$$

where the specific humidity at saturation is linearized around the mean land-surface deterministic temperature  $\overline{T}_{s_0} = T_{\text{deep}}$ .

[39] 6. The last boundary condition is the perturbation land-surface energy budget is

$$B_{T_{\text{day}}}(t) - 4\epsilon_s S T_{\text{deep}}^3 T'_{s_0} - G'(0) = \rho C_p \phi'_\theta(h) + \rho \lambda \phi'_q(h). \quad (15)$$

[40] The system behaves like it is forced by a new incoming radiation in the form of the Brownian bridge, around the same deterministic solution.

### 2.6.2. Perturbation Profiles

[41] As in the deterministic case presented by *Gentine et al.* [2010], the steady state solution should be derived first in order to express the full harmonic solution. The steady state equations are analogous to their deterministic equivalents. The steady state stochastic solutions represent the random biases in the daily mean values. Using the soil and temperature equations (see Figure 1), the steady state stochastic soil temperature and heat flux solutions are given in brackets representing the steady state value of the stochastic processes:

$$\langle G'(z) \rangle = 0, \quad (16)$$

$$\langle T'_s(z) \rangle = \langle T'_{s_0} \rangle. \quad (17)$$

Consequently, there is no diurnal random bias in the soil heat flux because its steady state component is zero; that is, there is no mean daily bias induced by the energy budget noise at the land surface. This result is dependent on the spectrum of the noise (discussed next). The components and ABL profiles of the steady state solution are described in Appendix A, section A1. The harmonic solution is derived in the same way as the one introduced by *Gentine et al.* [2010] except that the forcing harmonics of net radiation are replaced by the harmonics of the BB.

[42] The harmonics are presented at all frequencies. The Nyquist frequency is not limiting since the Brownian bridge is expressed as a full Fourier series that includes all daily harmonics. With these harmonics the profiles induced by the BB at the surface can be analytically derived. They are expressed as linear transformation of the harmonics of the BB. These harmonics are Gaussian random variables. The statistics of system variables within the soil-vegetation-ABL continuum can be analytically derived based on them.

### 2.6.3. Time Varying Variance and Correlations

[43] Because all soil and ABL variables are linear transformation of the BB harmonics, the time varying covariance between two variables can be expressed as a Fourier series using the covariance of their Fourier coefficients:

$$\begin{aligned} \text{cov}(X(t), Y(t)) &= \text{cov}(\langle X_0 \rangle, \langle Y_0 \rangle) \\ &+ 2\text{Re} \left[ \sum_{n=1}^{+\infty} \left( \text{cov}(\langle X_0 \rangle, \widetilde{Y}_n) + \text{cov}(\langle Y_0 \rangle, \widetilde{X}_n) \right) \right. \\ &\left. \cdot \exp(-j\omega_n t) + \text{cov}(\widetilde{X}_n, \widetilde{Y}_n) \right]. \quad (18) \end{aligned}$$

In particular the variance of any stochastic process will be expressed as:

$$\begin{aligned} \text{var}(X(t)) &= \text{var}(\langle X_0 \rangle) \\ &+ 2\text{Re} \left[ \sum_{n=1}^{+\infty} 2\text{cov}(\langle X_0 \rangle, \widetilde{X}_n) \exp(-j\omega_n t) + \text{var}(\widetilde{X}_n) \right], \quad (19) \end{aligned}$$

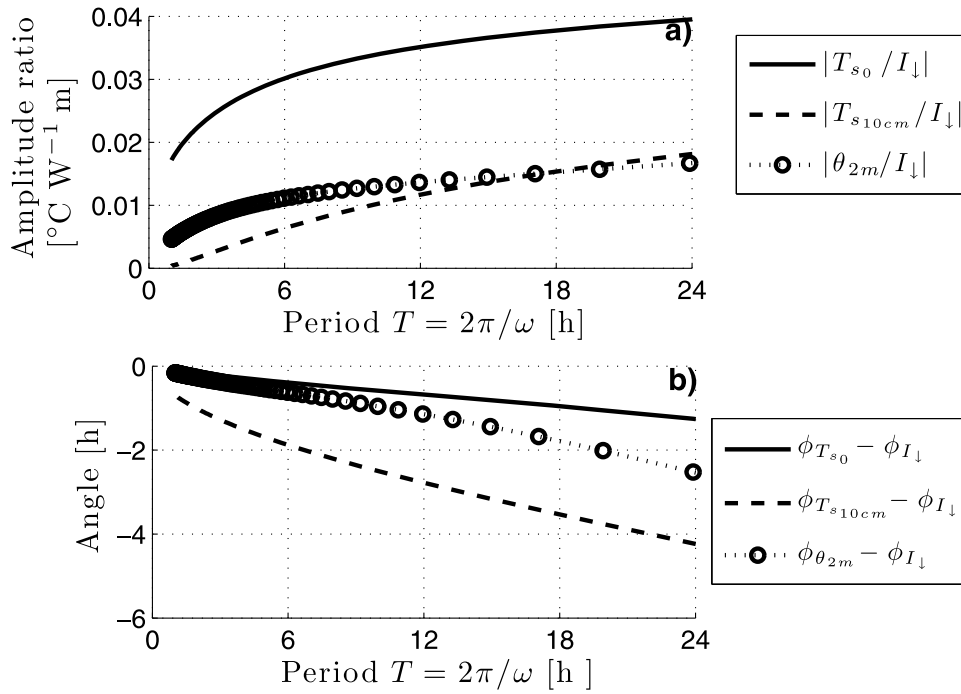


**Figure 7.** (a) Gain and (b) phase spectra of the land-surface (solid line), 10 cm deep (dashed line), and screen-level (circles) temperatures relative to incoming radiation  $I_{\downarrow}$  as a function of the period  $T = 2\pi/\omega$  of the forcing.

and the cross-correlations are given by:

$$\text{cov}(X(t), Y(t - \tau)) = \text{cov}(\langle X_0 \rangle, \langle Y_0 \rangle) + 2\text{Re}F(t), \quad (20)$$

where

$$F(t) = \sum_{n=1}^{+\infty} \left[ \left( \text{cov}(\langle X_0 \rangle, \tilde{Y}_n) \exp(-j\omega_n(t - \tau)) \text{cov}(\langle Y_0 \rangle, \tilde{X}_n) \right) \cdot \exp(-j\omega_n t) + \text{cov}(\tilde{X}_n, \tilde{Y}_n) \exp(-j\omega_n \tau) \right]. \quad (21)$$

The correlations can then be described analytically. These expressions are the foundations for understanding the influence of the land-surface energy balance variability on the soil and ABL scalars and fluxes.

[44] The fundamental characteristic of the harmonic solution is that the phase of the Fourier coefficients of the process is random; that is, they are uniformly distributed. Indeed, the coefficients of the BB error forcing are uncorrelated with their own conjugate, leading to the independence of the real and imaginary part of the normally distributed coefficient. Since soil and atmosphere variables are linear combinations of the land-surface forcing (the Fourier coefficients of the BB), their Fourier coefficients exhibit a random and uniformly distributed phase. This result has important consequences. The effect of high-frequency (or low-frequency) noise is uniformly distributed throughout the day. In the deterministic case a given harmonic of incoming solar radiation forcing had an associated phase lag. This illustrates a fundamental difference between the stochastic and deterministic solutions with significant impacts on

the response of the land-atmosphere coupled system to land-surface energy balance variability.

### 3. Results

#### 3.1. Land-Surface Temperature

[45] Since the LST is the principal coupling between the soil medium and the ABL within the soil-vegetation-atmosphere continuum, we first focus on its response to radiative forcing. The response of the complex amplitude of the LST to incoming radiation forcing is shown in Figure 7. In response to incoming radiative heating, the LST ( $T_{s_0}$ ) rises with a delay induced by the large-magnitude heat capacity of the soil. Because of the LST inertia, the LST phase increases at high-frequency (low period  $T$ ) forcing and is accompanied by a reduced amplitude response (Figure 7). Consequently, the LST acts as a low-pass filter of the incoming radiation forcing. Even though the LST tends to amplify the lowest daily frequencies of the radiative forcing, the high-frequency amplitude response is not negligible and is of the order of half the daily frequency ( $T = 24$  h). Therefore, rapid changes in solar incoming radiation (e.g., passing clouds), as observed in Figure 4, can lead to important modification in the LST, as shown in the surface infrared temperature time series of Figure 5.

#### 3.2. Surface Heat Fluxes

[46] The LST responds to incoming radiation fluctuations, and the perturbations are dissipated through turbulent fluxes, outgoing thermal radiation, and soil heat fluxes.

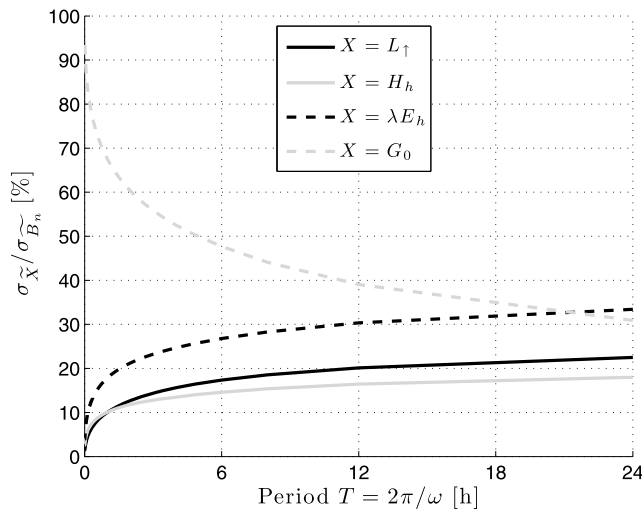


**Figure 8.** Standard deviation of the harmonics of the surface heat fluxes (outgoing radiation, sensible, and latent and soil heat fluxes) relative to the standard deviation of the period of the Brownian bridge harmonics as a function of the period  $T = 2\pi/\omega$ .

Figure 8 shows that the high-frequency (low period  $T$ ) variability of the land-surface noise mostly impacts the soil heat flux compared to the other components of the surface energy balance. Conversely, low-frequency (high period  $T$ ) land-surface noise mostly influences turbulent heat; that is, stochasticity of forcing on these timescales is mostly dissipated through turbulent heat fluxes. This behavior is comparable to the deterministic case presented in the previous section: the deterministic soil heat flux was shown to dominate in passing, as a filter, the high frequencies in solar incoming radiation forcing. When forced by stochastic noise, soil heat flux plays an equivalent role and mostly passes high-frequency (low period  $T$ ) noise. Turbulent heat transfer and longwave surface outgoing radiation  $L_{\uparrow}$  are less efficient than ground heat flux at high frequencies. Soil heat flux compensates for this attenuation and balances the energy budget at the land surface at these frequencies. Therefore, soil heat flux responds more rapidly to high-frequency incoming radiation forcing, and it is in phase advance with respect to incoming radiation. This represents a counterintuitive result since turbulent heat dissipation is a faster process than soil heat diffusion. The rapid LST changes create a steep soil surface temperature gradient since deeper soil temperatures with larger inertia do not have time to adjust as rapidly. On the other hand the rapid and efficient propagation of heat in the ABL quickly readjusts the temperature profile. Consequently, the ABL temperature gradients are reduced. In turn, they reduce the sensible heat flux. If the changes in LST are slower (at lower frequency), these modifications have sufficient time to propagate into the soil so that the soil heat flux is reduced and most of the dissipation of heat happens through other processes, namely, turbulent and radiative heat dissipation.

[47] The soil heat flux steady state solution is zero; that is, there is no diurnal bias. Consequently, the land-surface energy budget noise does not bias soil heat flux, but it does bias other fluxes. This result is linked to the linearization as well as to the color of the noise: with a different spectral

repartition of the noise at the land surface this result could change. Monte Carlo numerical simulations (not shown) indicate that this result is relatively insensitive to the color of the noise, and soil heat flux remains unbiased since it always acts as a high-pass filter of the noisy forcing.

[48] The cumulated spectrum of the heat fluxes (not shown) further confirms this behavior. The spectrum of outgoing longwave radiation  $L_{\uparrow}$  mostly passes low- and medium-frequency diurnal noise, as shown in Figure 8. It is less sensitive to high-frequency noise such as those in incoming radiation (e.g., passing clouds). Similar to LST, even though outgoing radiation acts as a low-pass filter, the high-frequency (about 5 min) response is nevertheless nonnegligible (about 10%–20% of the lowest daily frequency). In the case of rapid solar radiation spikes of about  $50\text{--}100\text{ W m}^{-2}$  at about 1–5 min resolution, this could lead to errors of about  $5\text{--}20\text{ W m}^{-2}$ . This translates to  $0.8\text{--}3.2\text{ K}$ , which is in good agreement with observations (see Figure 5).

[49] Turbulent heat fluxes respond similarly. The overall gain spectra of these fluxes are mostly contained in the lower frequencies. They are influenced by high-frequency noise. Land-surface noise thus reverberates, through mostly on middle and low frequencies.

[50] Soil heat flux behaves much differently: its noise spectrum is mostly influenced by high-frequency noise. The contribution of the low frequencies to the total variance is almost negligible. This indicates that measurement protocols and modeling requirements for soil heat flux at the surface need considerable improvements and care. Current approaches to the determination of soil heat flux, by in situ observations or numerical models, are inadequate and a source of considerable error in energy budget closure. Improvements in the methodology of current soil heat flux measurements will be discussed in a forthcoming study. This pivotal role of soil heat flux was emphasized some 30 years ago by Deardorff [1978, pp. 1889–1903], where he warned that “any assumption [on  $G$ ] that it is proportional to any particular component, or partial set of such components, seems dangerously non-general.” Applications that take  $G$  as a fraction of net radiation may introduce significant phase and amplitude errors in the surface energy balance.

### 3.3. Temperature Profiles in the Lower Surface Layer and Soil

[51] The ABL and soil profiles of the temperature gain spectra relative to LST are displayed in Figure 9. They are plotted as a function of the period  $T$  of the incoming radiation forcing. The profiles of interest extend up to 10 m in the ABL (lower surface layer) and to 0.5 m deep into the soil (limit of the diurnal heat wave penetration), even though the model extends to the ABL top and far-field into the soil. Again, we intentionally limit our presentation to only 10 m above the surface in order to remain in a region where the assumptions profile stability and fixed ABL height are valid. The values of the heights and depths beyond these limited regions are dependent on the surface and environmental conditions.

[52] Response to high-frequency forcing remains condensed in a very shallow layer of the soil (of about 10 cm in our experiment, but this value will vary according to soil properties), and it also affects a very shallow region of the ABL (of about 5 m in our case). Consequently, the

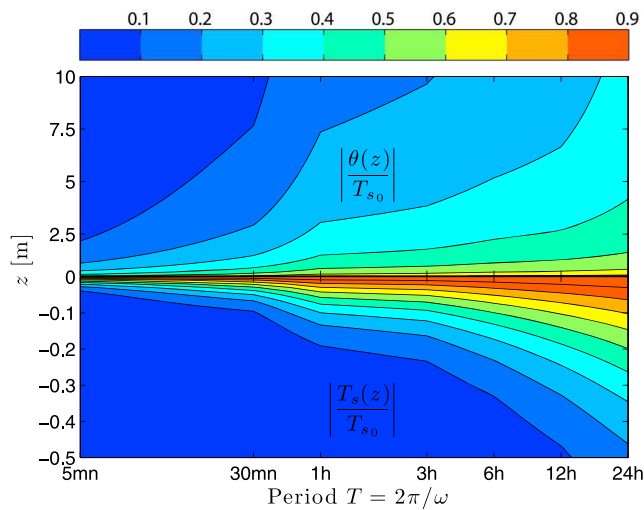


**Figure 9.** Gain contours (top) for potential temperature as a function of height and (bottom) for soil temperature as a function of depth, relative to land-surface temperature.

profiles of temperatures farther from the surface in the land-atmosphere system are mostly influenced by low-frequency daily forcing of incoming radiation. The near-surface soil temperature harmonics have larger amplitudes compared to the near-surface ABL temperatures. In fact, the LST changes have a lower impact on the air temperature than on the subsurface soil temperature because of the strong discontinuity of heat properties between the land surface and the air.

[53] The phase contours depicted in Figure 10 yield insight into the propagation speed of a LST spike into the soil-vegetation-atmosphere continuum. At lower frequencies (high periods  $T$ ) there are relatively less delays between the temperature responses in the surface layer and the LST. At high frequencies (low periods  $T$ ), only the very bottom of the surface layer ( $z \leq 3$  m in our experiment) experiences short delay with the LST changes. Above that height the surface layer experiences more phase delay. This delay is almost uniform at low frequencies throughout the near-surface ABL, consistent with the fact that the sensible heat flux propagates from the surface almost instantaneously into the lower ABL. On the other hand, the soil medium experiences more phase delay, as evident in Figure 10 (bottom). Again, this is due to the relative inefficient heat diffusion in the soil when compared to the ABL. This strong delay in the response of the deeper soil temperatures to surface radiative forcing induces a very steep surface gradient at the land surface at high frequencies. The frequency dependence of this phenomenon is key to explaining the relative efficiency of the surface energy balance components as a function of period and type of noise. This was evident in Figure 5, and it will be further illustrated using a frequency-dependent resistance analogy in section 4.

[54] Figure 11b shows the response of the temperature harmonics relative to the harmonics of the BB (Figure 11a). In essence the response is similar to the deterministic case, as one would expect from the equivalent formulation of the harmonics in the stochastic and deterministic cases. Yet the spectral repartition of the BB (Figure 11a) is fundamentally different from the deterministic forcing of incoming radiation. The spectrum of incoming radiation is composed of

one main diurnal harmonic at  $T = 24$  h and a smaller semidiurnal one at  $T = 12$  h, under fair weather conditions. The other harmonics have negligible amplitude. Consequently, the behavior of the soil and ABL as linear filters in the frequency domain is not as important in the deterministic formulation as it is for the stochastic formulation. In the stochastic formulation the forcing has a broader and richer spectrum.

[55] The absolute response of the temperature to the noise forcing is obtained through the multiplication of the spectrum of the BB (Figure 11a) with the gain spectrum (Figure 11b). The LST acts as a low-pass filter of the forcing, which is mostly influenced by the low-frequency component of the energy budget noise. Indeed, in the case of the BB, 98% of the noise in the LST is distributed above period  $T \geq 6$  h (not shown). In the case of a redder noise, the high-frequency spectrum would have a larger contribution to the total surface variability.

[56] The potential temperature at 2 m behaves similarly to the LST in the sense that it preferentially passes the middle-to-lower-frequency part of the noise spectrum. In the case of the BB, more than 99.5% of the noise is distributed at periods  $T \geq 12$  h and more than 96.5% of the noise is distributed at periods  $T \geq 24$  h. This has fundamental implications since it signifies that the impact of the noise in the lower ABL temperatures is mostly present in the form of a daily bias (period  $T \rightarrow \infty$ ).

[57] The soil temperature at 10 cm below the surface significantly filters the effect of high-frequency noise, and almost all the variability is at periods higher than 12 h and 99% of the noise if located at periods  $T \geq 24$  h. This shows that the noise induced by energy budget errors at the land surface also takes the form of a daily bias in the deeper temperatures. These results quantify the band-pass filter characteristics of the temperatures both in the ABL and in the soil.

#### 4. Physical Interpretation: Circuit Analogy

[58] The basic response of the ABL and soil temperature profiles and that of the surface heat fluxes can be captured in

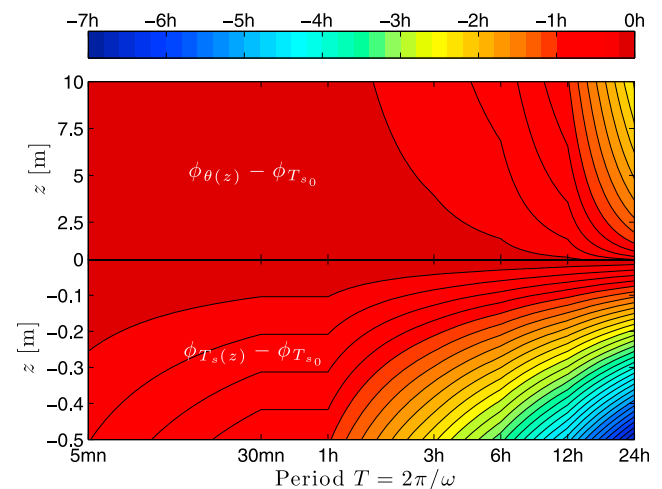


**Figure 10.** Phase contours (top) for potential temperature as a function of height and (bottom) for soil temperature as a function of depth, relative to land-surface temperature.

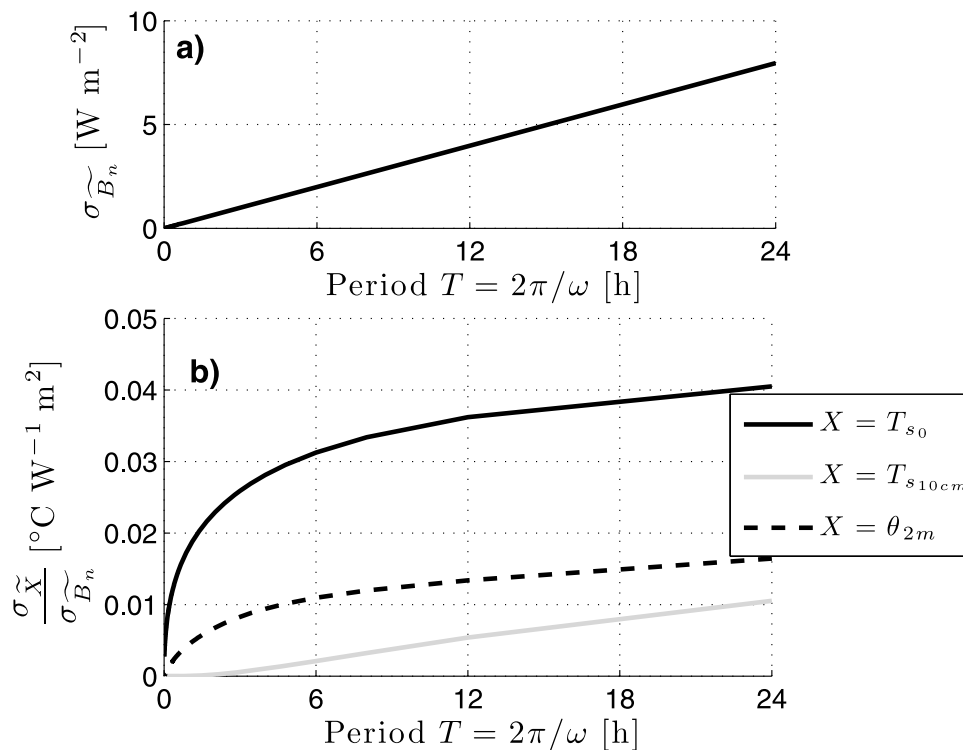


**Figure 11.** Standard deviation of the harmonics of (a) the Brownian bridge and (b) the temperatures relative to the standard deviation of the Brownian bridge harmonics, as a function of the period  $T = 2\pi/\omega$ .  $T_{s_0}$  represents the land-surface temperature,  $T_{s_{10cm}}$  represents the soil temperature at 10 cm, and  $\theta_{2m}$  represents the potential temperature at 2 m in the boundary layer.

a simple meta-model that illustrates the essential behaviors. The analogy is particularly useful in explaining the dominance of ground heat flux over turbulent fluxes in dissipating high-frequency noise in surface energy balance. An electrical circuit is used to illustrate the physical response of the coupled system at different frequencies. Its basic schematic is shown in Figure 12 (omitting conductances). The circuit representation is solved using Mathworks© Simulink. The details are contained in Appendix B. The LST is connected to the potential temperature at canopy height  $\theta_h$  through a small resistance  $r_a^c$  induced by surface turbulence. This latter temperature is linked to the potential temperature at the bottom of the mixed layer  $\theta_{ML}$  through another small (surface layer) aerodynamic resistance  $r_a^{SL}$ . The temporal derivative controlling the changes in temperatures, which are modeled by capacitances, are not depicted in Figure 12 for the sake of legibility. The potential temperature within the mixed layer displays little vertical gradients and is assumed to be uniform and to adjust freely (schematic representation in Figure 12 (top)). In essence, such a diagram corresponds to slab models of the boundary layer as used by Tennekes [1973], Deardorff [1979], Troen and Mahrt [1986], and Brubaker and Entekhabi [1995], except that the temperatures at vegetation height  $\theta_h$  are also accounted for in the formulation. In this diagram the heat fluxes are given by the voltage differences across the resistances. Now the repercussions of a rise in LST can be investigated within the ABL and the soil media. The controlling parameters can be identified.

[59] The soil media representation requirements are fundamentally different than those of the ABL. High resolution

is required in the first few centimeters of the soil in order to account for strong surface gradients induced by the low diffusion coefficients and high heat capacity. The first 5 cm of soil are thus divided into five homogeneous 1 cm deep sublayers, then below 5 cm, a soil layer of 5 cm is considered. The temperature at 10 cm is coupled with a temperature deep in the soil  $T_{deep}$ , through a resistance  $r_s^{deep}$ . Deeper in the soil the gradients of soil heat flux are assumed to be negligible (schematic representation in Figure 12 (bottom)).

[60] This formulation is, in essence, different from the force-restore formulation of the evolution of soil temperatures [see, e.g., Hu and Islam, 1995; Mihailovic et al., 1999; Jacobs et al., 2000; Savijarvi, 1992; Dickinson, 1988] and represents a discretization of the soil diffusion equation. High-frequency response of the soil would be truncated with coarser soil surface discretization. For example, a large (e.g., 5 cm) grid size at the topmost node of the soil temperature profile, as commonly used in operational land-surface schemes, filters out much of the important high-frequency (low period) variability identified in this study.

[61] Figure 12 shows a schematic representation of the high-frequency (Figure 12a) and low-frequency response of the coupled land-atmosphere system (Figure 12b). When LST rises in response to a high-frequency (low period  $T$ ) forcing in surface radiation, the soil and ABL behave very differently (see Figure 7). Since the heat resistances in the ABL are much lower than their soil counterparts, the potential temperatures in the lower ABL rapidly adjust to a change in LST. The ABL temperatures rapidly reach a state of equilibrium, with fast internal feedbacks. Conversely,

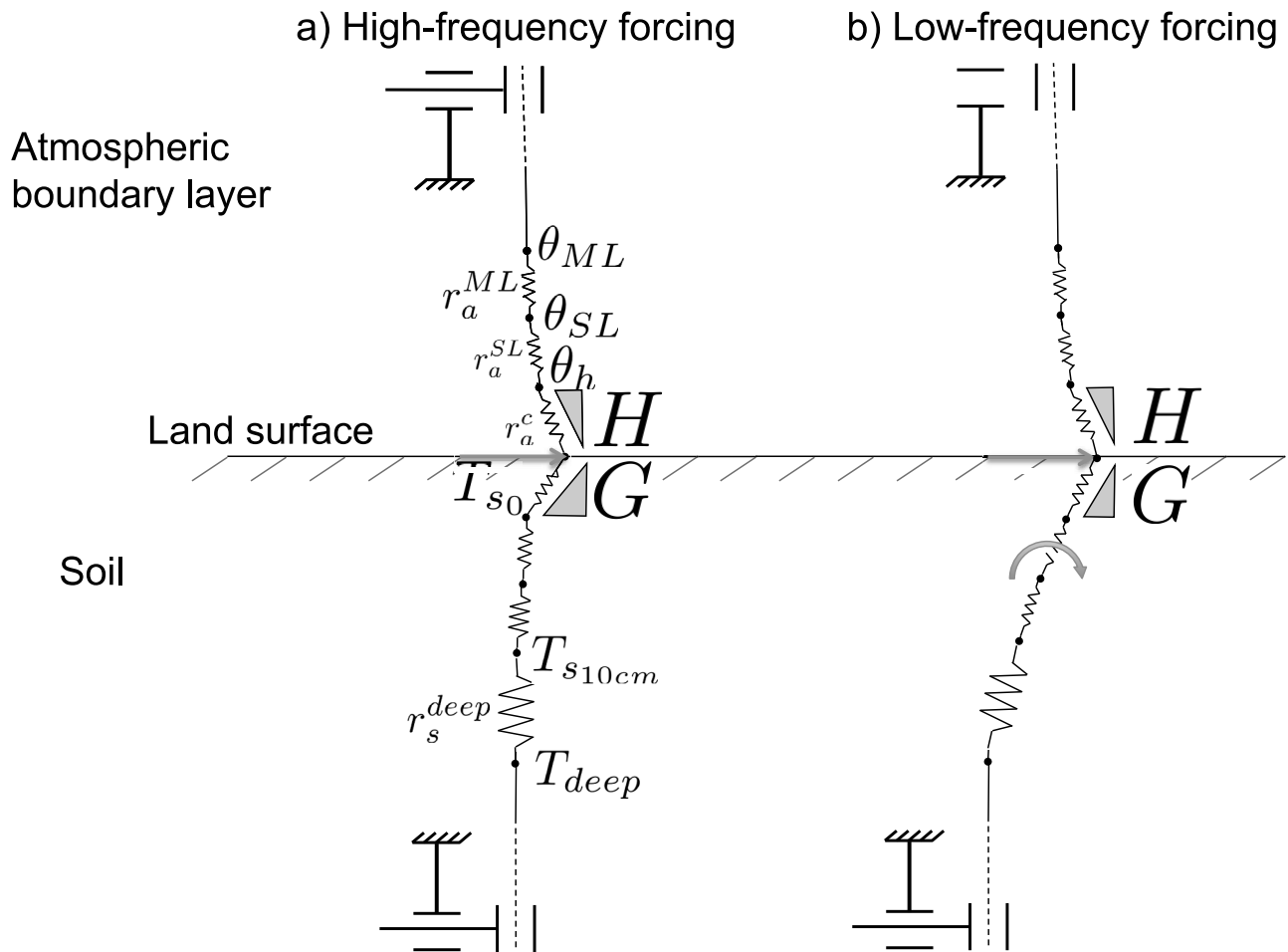


**Figure 12.** (top and bottom) Schematic resistance diagram of the surface heat flux and temperature response to variability in LST induced by (a) high-frequency and (b) low-frequency forcing. Land-surface temperature  $T_{s_0}$  is the trigger of the coupled system, as emphasized by the horizontal arrow. The potential represents the temperatures, and the slope of the resistances represents the intensity of the heat fluxes. In the low-frequency case (Figure 12b), the deeper temperatures have time to adjust to land-surface temperature modifications, leading to smoother and more penetrating gradients of soil temperature.

the high-frequency LST forcing does not have time to propagate deep into the soil because of the inefficient heat diffusion in the soil medium. The temperatures deeper in the soil are less affected since they do not have time to adjust to the rapid high-frequency LST changes. In turn the surface slope of the soil surface resistance is large since the deeper temperatures cannot track the high-frequency LST changes. This results in a large-magnitude, rapid soil heat flux induced by high-frequency (low period  $T$ ) noise in surface energy balance. The coupling of the unperturbed temperature at 10 cm on the LST leads to a feedback and restore effect (as in the force-restore formulations), which limits the rise of the LST induced by high-frequency radiative forcing, as depicted in Figure 7.

[62] The response to low-frequency (high period  $T$ ) radiative forcing is fundamentally different, as depicted in Figure 12b. In response to this forcing, the LST rises. The ABL is again able to adjust quickly in the case of the high-frequency forcing because of the efficient turbulent transport of heat and because of the low heat capacity of the air. However, the response of the soil is fundamentally different

at low frequencies. Since the LST change is slow (low frequency), the temperature deeper in the soil  $T_{s_{10cm}}$  has sufficient time to track the LST modifications. Consequently, the slope of the soil resistance between  $T_{s_0}$  and  $T_{s_{10cm}}$  is reduced in the case of low-frequency (high period  $T$ ) radiative forcing and is of the same order as the atmospheric slope between  $T_{s_0}$  and  $\theta_h$ . This behavior corresponds well to the response of the soil and sensible heat fluxes (Figure 13, left), which is for the linearized soil-vegetation-atmosphere continuum model.

[63] This effect is further confirmed by Figure 13 (right) using the circuit representation of the heat fluxes in response to LST changes. In this experiment the amplitude of the LST forcing is constant at 10 K. The response of the soil heat flux is highly dependent on the frequency, whereas the response is similar at all frequencies for sensible heat flux. This confirms that the transport of heat in the ABL is so rapid so that the sensible heat flux is similarly sensitive to both high- and low-frequency changes. In contrast, soil heat flux response is more significant at high frequencies since the heat does not have time to propagate into the soil, leading to

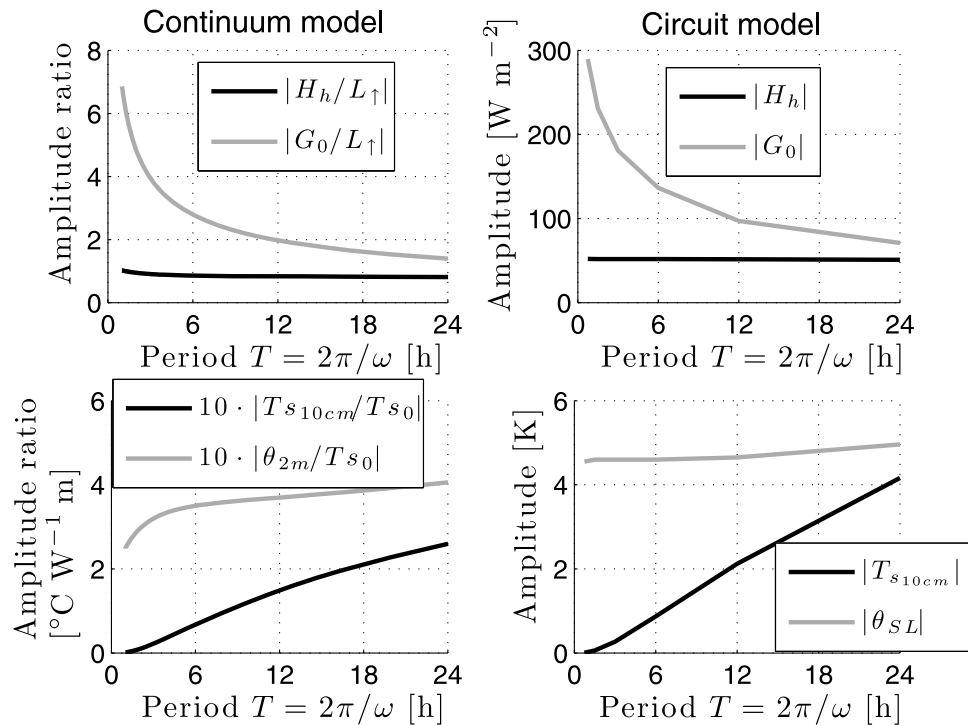


**Figure 13.** (top) Gain spectra of sensible and soil heat flux and (bottom) soil temperature at 10 cm and potential temperature at 2 m as a function of the period  $T$  of the incoming radiation forcing, using (left) the linearized soil-vegetation-atmosphere model and (right) the circuit model.

a concentration of the gradients in the upper soil layer. The behavior of the soil-vegetation-atmosphere continuum model in Figure 13 (left) is to be compared with the circuit response in Figure 13 (right). Since the circuit is forced with a 10 K uniform spectrum of LST, the soil-vegetation-ABL continuum sensible and ground heat flux gain spectra with respect to LST needs to be constructed and compared. Here we use outgoing thermal radiation, which is directly proportional to LST, to have the same units as  $G$  and  $H_h$ . Figures 13 (left) and 13 (right) show similar patterns of dependence of sensible and ground heat flux gain spectra with respect to LST.

[64] One additional comment can be made regarding the low- versus high-frequency (high versus low period  $T$ ) response of the turbulent and radiative fluxes. As stated in section 3.3, modifications of LST due to surface energy balance variability are the gateway for responses in the remainder of the system. Yet it has been shown that at high frequency (low period  $T$ ) the temperature deeper in the soil ( $T_{s_{10cm}}$ ) exerts a strong coupling and feedback on  $T_{s_0}$ , consecutively limiting the rise of near-surface soil temperature and turbulent heat fluxes. This explains why the amplitude of the surface temperatures (Figure 7) as well as radiative and turbulent fluxes (not shown) are reduced at higher frequencies (lower period  $T$ ).

[65] These results point to a potential limitation of the classical force-restore soil thermal model [see, e.g., *Hu and Islam, 1995; Mihailovic et al., 1999; Jacobs et al., 2000; Savijarvi, 1992; Dickinson, 1988*]. The restoring term at lower daily frequencies should be less than the value at higher frequencies. The restoring term and its parameterization are thus fundamentally dependent on the frequency of the forcing.

[66] In the ABL the opposite behavior is observed. Sensible heat flux response at the surface has greater gain at low frequencies compared to the higher frequencies. Because the forcing is slow compared to the efficient turbulent transport of heat, the whole ABL has sufficient time to adjust to LST changes at all frequencies. This indicates that the use of slab models of the ABL coupled to LST provide physically sound responses at low and high frequencies.

## 5. Sensitivity to Fixed Parameters

[67] The results of this study are limited by the assumptions made for the values of key parameters. These include friction velocity  $u_*$ , canopy aerodynamic resistance  $r_a^c$ , water availability  $\beta$  (evaporative control), soil thermal diffusivity  $K_s$ , soil heat capacity  $C_s$ , vegetation height  $h$ , surface albedo  $\alpha_s$ , and emissivity  $\epsilon_s$ .

[68] In order to address at least the sensitivity of the model outputs to the values of these parameters, a basic simulation study is performed where the elasticity of the main model states and fluxes are evaluated. Here elasticity refers to percent change in an output as a result of a percentage change in a model parameter. Specifically, we focus on the main model parameters, that is, water availability  $\beta$ , soil heat diffusivity  $K_s$ , and friction velocity  $u_*$ .

[69] The sensitivity of the surface temperatures and heat fluxes to a change in water availability  $\beta$  are listed in Table 1 as a function of the period  $T$  of the forcing. An increase in  $\beta$  leads to a decrease in the variability of all temperatures and fluxes but latent heat flux. As expected, latent heat flux is directly influenced by a change in water availability, at all frequencies. Soil heat flux variability is only slightly reduced with  $\beta$  increase. Water availability is

**Table 1.** Sensitivity of the Standard Deviation of the Surface Temperatures and Heat Fluxes to a Change in Water Availability  $\beta^a$ 

$\frac{\Delta\sigma_x}{\sigma_x} / \frac{\Delta\beta}{\beta}$	$T = 1 \text{ h} (\%)$	$T = 6 \text{ h} (\%)$	$T = 24 \text{ h} (\%)$
$T_{s_0}$	-6.87	-8.47	-9.97
$\theta_{2m}$	-6.85	-8.45	-9.97
$T_{s_{10cm}}$	-6.85	-8.46	-9.98
$H_h$	-6.86	-8.47	-9.98
$\lambda E_h$	32.77	24.12	20.31
$G$	-6.86	-8.47	-3.08

<sup>a</sup>Table 1 contains the harmonic response of the standard deviation as a function of the period  $T$ . Sensitivities are expressed as logarithmic changes over the logarithmic change in water availability (dimensionless).

mainly sensitive to root zone soil moisture, and variations of less than 5% were observed during the SudMed experiment, except right after rainfall and irrigation. A 5% modification in  $\beta$  would lead to changes below 0.5% for all temperatures and fluxes except latent heat. At the daily time scale the variability in latent heat flux would change by only 1%, thus emphasizing that the daily variations in water availability will not appreciably affect the results presented in this study.

[70] The soil diffusivity has a stronger influence on almost all variables, as demonstrated on the sensitivity Table 2. Soil diffusivity has a large impact on the soil temperature at 10 cm since an increase in  $K_s$  permits propagation of variability deeper in the soil. The variability in other components is reduced since more energy is conducted from the surface by the increase in the soil conductivity. Observed typical diurnal variations of soil moisture of about 5% lead to a change of 1% in land-surface temperature, potential temperature at 2 m, and turbulent heat fluxes. The variability in soil heat flux will be modified by about 2.5%. The soil temperature at 10 cm is much more impacted in relative value since its absolute value is very close to zero; consequently, its amplitude change may be small in absolute value.

[71] Friction velocity certainly is the most significant surface parameter controlling the turbulent heat fluxes at the land surface. Table 3 presents the sensitivity response of the surface temperatures and heat fluxes to friction velocity. An increase in friction velocity leads to a strong reduction in the variability of all temperatures because of the intensified turbulent dissipation and redistribution. As expected, the increase in the variability of sensible heat flux is the most important, especially compared to latent heat in our non-water limited case. The increased variability in surface turbulent heat fluxes is partly compensated by the reduced

variability in soil heat flux. Since friction velocity can have typical variations of 100% during the course of the day, it is clear that the constant friction velocity assumption is a shortcoming of the model used in this study. A time varying friction velocity results in a nonlinear model (see Figure 1) and precludes an analytical solution. Without an analytical solution to the problem, the interpretation of the system response in terms of gain and phase harmonics becomes difficult. Friction velocity can vary over the course of a day as a result of passing synoptic systems and nonstationary turbulence. Using the same SudMed observations as by *Gentine et al.* [2010], we estimated the statistical power spectrum of friction velocity using 70 days of turbulence measurements (not shown). The spectrum of friction velocity is broad, and there is only one main peak at  $T = 24 \text{ h}$  (not shown). However, the relative response of all harmonics is small compared to the mean diurnal value. Over the 70 days of turbulent heat flux observation, 73% of the daily power spectrum of friction velocity is concentrated in the mean daily average, and 93% of its daytime hours power spectrum is concentrated in the daytime mean value. Consequently, the assumptions about this important and sensitive parameter may be limiting but are unlikely to have impacted the core conclusions.

## 6. Conclusion

[72] In this study, the harmonic responses of the land-surface energy balance components, soil temperature profile, and near-surface ABL temperature and humidity profiles to radiative forcing and surface energy budget variability are investigated using a model of the soil-vegetation-atmosphere continuum. The heat fluxes in the continuum are a function of the gradients in state (e.g., temperature) profiles. The amplitude gain and phase spectra are derived in order to quantify the spectral characteristics of the propagation of variabilities in the system.

[73] In a second part of this study we focus on the impact of energy budget variability. A richer land-surface forcing spectrum consisting of a stochastic forcing is considered. Since soil heat flux is a high-frequency band-pass filter of the noise, it preferentially passes the higher frequencies leading to short memory and strong variability in response to high frequency. Turbulent heat fluxes are, on the other hand, mostly influenced by the low-to-middle portions of the noise spectrum. They can produce daily bias if under-sampled. Even though the land-surface temperature responds more vigorously to the lowest daily frequencies, high frequencies are nonnegligible and rapid variations of about

**Table 2.** Sensitivity of the Standard Deviation of the Surface Temperatures and Heat Fluxes to a Change in Soil Diffusivity  $K_s^a$ 

$\frac{\Delta\sigma_x}{\sigma_x} / \frac{\Delta K_s}{K_s}$	$T = 1 \text{ h} (\%)$	$T = 6 \text{ h} (\%)$	$T = 24 \text{ h} (\%)$
$T_{s_0}$	-42.96	-31.26	-20.81
$\theta_{2m}$	-42.96	-31.25	-20.82
$T_{s_{10cm}}$	887.07	171.75	65.97
$H_h$	-42.96	-31.26	-20.81
$\lambda E_h$	-42.96	-31.26	-20.81
$G$	22.09	38.63	53.41

<sup>a</sup>Table 2 contains the harmonic response of the standard deviation as a function of the period  $T$ . Sensitivities are expressed as logarithmic changes over the logarithmic change in soil diffusivity (dimensionless).

**Table 3.** Sensitivity of the Standard Deviation of the Surface Temperatures and Heat Fluxes to a Change in Friction Velocity  $u_*^a$ 

$\frac{\Delta\sigma_x}{\sigma_x} / \frac{\Delta u_*}{u_*}$	$T = 1 \text{ h} (\%)$	$T = 6 \text{ h} (\%)$	$T = 24 \text{ h} (\%)$
$T_{s_0}$	-9.36	-19.15	-25.67
$\theta_{2m}$	-38.29	-49.72	-58.20
$T_{s_{10cm}}$	-9.36	-19.15	-25.67
$H_h$	53.41	53.80	49.03
$\lambda E_h$	20.65	20.17	15.55
$G$	-9.36	-19.15	-25.67

<sup>a</sup>Table 3 contains the harmonic response of the standard deviation as a function of the period  $T$ . Sensitivities are expressed as logarithmic changes over the logarithmic change in friction velocity (dimensionless).

50 W m<sup>-2</sup> in solar radiation (as typically observed in intermittent cloudy weather conditions) can lead to a 1 K modification of the land-surface temperature. Finally, the temperature at screen level (2 m) is less sensitive to the middle and high frequencies of the noise when compared to sensible heat flux. It is thus a relatively reliable boundary condition of the lower atmosphere in the presence of misrepresentations or errors at the land surface.

[74] A simple circuit analogy is developed to provide further insights into the physical responses of the continuum model to noise at the land surface as a function of frequency. This reduced model is easy to understand and provides a fundamental intuitive conceptualization of the problem. The soil and the near-surface ABL temperature states display fundamentally different behaviors at low or high daily frequencies, as evident in the circuit analogy because of the couplings and resistances. The resistances and capacitances in the circuits result in different band-pass filters for each of the states. In particular, the deep soil temperature exerts strong feedback (restoring term) on the subsurface temperature ( $T_{s_{10cm}}$ ) at low frequencies. At high frequencies the near-surface temperature, which is less constrained by the deep temperature, limits the fluctuations in LST. Conversely, the ABL displays stronger turbulent heat fluxes in response to low-frequency forcing. Most of the ABL is capable of responding with small phase differences to LST changes.

[75] The model here has inherent limitations; nevertheless, it serves well to provide insights into the propagations of variability that have different time scales of fluctuation. The soil-vegetation-ABL model is linearized in order to allow harmonic solution. This limits the model to the near-neutral stability regime in the atmosphere, and it also limits characterization of heterogeneities in soil and ABL parameters.

[76] The roles of signal-to-noise ratio in the deterministic and noisy characterization of radiative forcing, and other complexities in environmental conditions, may significantly impact the quantitative amplitude gain and phase spectra. The effects of these factors should be evaluated using numerical models with fine discretization and with field observations with high-frequency temporal sampling.

## Appendix A: Stochastic Fourier Development

### A1. Steady State Stochastic Solution

[77] In the ABL, the following temperature and humidity steady state and random profiles are obtained (angle brackets represent the steady state):

$$\langle \theta' \rangle(z) = -\frac{\Phi_1}{Ku_*^c} [z + (d - z_i) \ln(z - d)] + \Phi_2, \quad (A1)$$

$$\langle q' \rangle(z) = -\frac{\Psi_1}{Ku_*^c} [z + (d - z_i) \ln(z - d)] + \Psi_2. \quad (A2)$$

The unknown coefficients  $\Phi_i$  and  $\Psi_i$  are random variables. Using both expressions of sensible and latent heat flux at the land surface (boundary conditions in section 2.6.1), the coefficients can be expressed as a function of the air temperature and specific humidity perturbations away from

deterministic equilibrium ( $\langle \theta' \rangle(z)$  and  $\langle q' \rangle(z)$ , respectively, at height  $z$ ):

$$\begin{aligned} \langle \theta' \rangle(z) - \langle \theta' \rangle(h) &= (\langle T_{s_0}' \rangle - \langle \theta' \rangle(h)) \underbrace{\frac{1}{Ku_*^c r_a^c} \left[ \frac{z-h}{z_i-h} - \frac{(z_i-d)}{z_i-h} \ln \left( \frac{z-d}{h-d} \right) \right]}_{\triangleq \alpha(z)}, \end{aligned} \quad (A3)$$

$$\begin{aligned} \langle q' \rangle(z) - \langle q' \rangle(h) &= (\gamma_{T_{\text{deep}}} \langle T_{s_0}' \rangle - \langle q' \rangle(h)) \underbrace{\frac{\beta}{Ku_*^c r_a^c} \left[ \frac{z-h}{z_i-h} - \frac{(z_i-d)}{z_i-h} \ln \left( \frac{z-d}{h-d} \right) \right]}_{\triangleq \beta\alpha(z)}. \end{aligned} \quad (A4)$$

[78] The stochastic surface steady state budget can be rewritten as a function of these solutions:

$$\begin{aligned} \langle B_0 \rangle - 4\epsilon_s S T_{\text{deep}}^3 \langle T_{s_0}' \rangle &= \frac{\rho C_p}{r_a^c} \frac{\langle T_{s_0}' \rangle - \langle \theta' \rangle(z_1)}{1 - \alpha(z_1)} \\ &+ \frac{\rho \lambda \beta}{r_a^c} \frac{\gamma_{T_{\text{deep}}} \langle T_{s_0}' \rangle - \langle q' \rangle(z_1)}{1 - \beta\alpha(z_1)}. \end{aligned} \quad (A5)$$

In order to solve the problem, the steady state stochastic soil temperature  $\langle T_{s_0}' \rangle$  has to be found first, and the random variables  $\langle q' \rangle(z_1)$  and  $\langle \theta' \rangle(z_1)$  should be specified. These two random variables are assumed to be jointly independent, independent from the land-surface noise, and normally distributed with respective distribution  $\langle \theta' \rangle(z_1) \sim N(0, \sigma_\theta^2)$  and  $\langle q' \rangle(z_1) \sim N(0, \sigma_q^2)$ , where  $\sigma_\theta^2$  and  $\sigma_q^2$  represent the daily-mean error of potential temperature and specific humidity at height  $z_1$ . In this study the height  $z_1$  is taken as  $z_i$ , the ABL height.

[79] All random variables are normally distributed, because all input variables are normally distributed and because the problem is linear. In particular the steady state soil temperature error can be written as  $\langle T_{s_0}' \rangle \sim N(0, \sigma_{T_{s_0}'}^2)$ . The variance of this random variable can easily be obtained using equations (A3), (A4), and (A5):

$$\sigma_{T_{s_0}'}^2 = \frac{\frac{\sigma_\theta^2}{12} + \sigma_\theta^2 \left[ \frac{\rho C_p}{r_a^c (1 - \alpha(z_1))} \right]^2 + \sigma_q^2 \left[ \frac{\rho \lambda \beta \gamma_{T_{\text{deep}}}}{r_a^c (1 - \beta\alpha(z_1))} \right]^2}{\left[ 4_s S T_{\text{deep}}^3 + \frac{\rho C_p}{r_a^c (1 - \alpha(z_1))} + \frac{\rho \lambda \beta \gamma_{T_{\text{deep}}}}{r_a^c (1 - \beta\alpha(z_1))} \right]^2}. \quad (A6)$$

[80] There is consequently a correlation between  $\langle \theta' \rangle(z_1)$  and  $\langle T_{s_0}' \rangle$ , and their covariance can be written as

$$\text{cov}(\langle \theta' \rangle(z_1), \langle T_{s_0}' \rangle) = \frac{\sigma_\theta^2}{1 + \frac{4_s S T_{\text{deep}}^3 r_a^c (1 - \alpha(z_1))}{\rho C_p} + \frac{\lambda \beta \gamma_{T_{\text{deep}}} (1 - \alpha(z_1))}{C_p (1 - \beta\alpha(z_1))}}. \quad (A7)$$

Similarly, between  $\langle q' \rangle(z_1)$  and  $\langle T_{s_0}' \rangle$

$$\text{cov}(\langle q' \rangle(z_1), \langle T_{s_0}' \rangle) = \frac{\sigma_q^2}{\gamma_{T_{\text{deep}}} + \frac{4_s S T_{\text{deep}}^3 r_a^c (1 - \beta\alpha(z_1))}{\rho \lambda \beta} + \frac{C_p (1 - \beta\alpha(z_1))}{\lambda \beta (1 - \alpha(z_1))}}. \quad (A8)$$

Finally, for  $\langle B_0 \rangle$  and  $\langle T'_{s_0} \rangle$

$$\text{cov}(\langle B_0 \rangle, \langle T'_{s_0} \rangle) = \frac{\frac{\sigma^2 T_{\text{day}}}{12}}{4_s ST_{\text{deep}}^3 + \frac{\rho C_p}{r_a^c (1-\alpha(z_1))} + \frac{\rho \lambda \beta \gamma T_{\text{deep}}}{r_a^c (1-\beta \alpha(z_1))}}. \quad (\text{A9})$$

These covariances are required to express the steady state variance of respectively sensible and latent heat:

$$\sigma_{\langle \theta_h \rangle}^2 = \frac{\rho C_p}{r_a^c} \left( \sigma_{T_{s_0}}^2 + \sigma_{\theta_h}^2 - 2 \text{cov}(\langle T'_{s_0} \rangle, \langle \theta_h' \rangle) \right), \quad (\text{A10})$$

$$\sigma_{\langle \lambda E_h \rangle}^2 = \frac{\rho \lambda}{r_a^c} \left( \gamma T_{\text{deep}}^2 \sigma_{T_{s_0}}^2 + \sigma_{q_h}^2 - 2 \gamma T_{\text{deep}} \text{cov}(\langle T'_{s_0} \rangle, \langle q_h' \rangle) \right), \quad (\text{A11})$$

where

$$\sigma_{\langle \theta_h' \rangle}^2 = \frac{\sigma_{\theta}^2 + \alpha^2(z_1) \sigma_{T_s}^2 - 2 \alpha(z_1) \text{cov}(\langle \theta(z_1)' \rangle, \langle T'_{s_0} \rangle)}{(1 - \alpha(z_1))^2}, \quad (\text{A12})$$

$$\sigma_{\langle q_h' \rangle}^2 = \frac{\sigma_q^2 + [\gamma T_{\text{deep}} \beta \alpha(z_1)]^2 \sigma_{T_s}^2 - 2 \gamma T_{\text{deep}} \beta \alpha(z_1) \text{cov}(\langle \theta(z_1)' \rangle, \langle T'_{s_0} \rangle)}{(1 - \alpha(z_1))^2}, \quad (\text{A13})$$

$$\text{cov}(\langle \theta_h' \rangle, \langle T'_{s_0} \rangle) = \frac{\text{cov}(\langle \theta(z_1)' \rangle, \langle T'_{s_0} \rangle) - \alpha(z_1) \sigma_{T_{s_0}}^2}{1 - \alpha(z_1)}, \quad (\text{A14})$$

$$\text{cov}(\langle q_h' \rangle, \langle T'_{s_0} \rangle) = \frac{\text{cov}(\langle q(z_1)' \rangle, \langle T'_{s_0} \rangle) - \beta \alpha(z_1) \gamma T_{\text{deep}} \sigma_{T_{s_0}}^2}{1 - \beta \alpha(z_1)}. \quad (\text{A15})$$

Then using the steady state relations

$$\langle \theta' \rangle(z) = \alpha(z) \langle T'_{s_0} \rangle + (1 - \alpha(z)) \langle \theta_h' \rangle, \quad (\text{A16})$$

$$\langle q' \rangle(z) = \beta \alpha(z) \gamma T_{\text{deep}} \langle T'_{s_0} \rangle + (1 - \beta \alpha(z)) \langle q_h' \rangle, \quad (\text{A17})$$

$$\langle \phi_{\theta}' \rangle(z) = \langle \phi_{\theta}' \rangle(h) \frac{z - z_i}{h - z_i}, \quad (\text{A18})$$

$$\langle \phi_q' \rangle(z) = \langle \phi_q' \rangle(h) \frac{z - z_i}{h - z_i}. \quad (\text{A19})$$

The steady state variances at any height are

$$\begin{aligned} \sigma_{\langle \theta(z) \rangle}^2 &= \alpha^2(z) \sigma_{T_{s_0}}^2 \\ &+ (1 - \alpha(z))^2 \sigma_{\theta_h}^2 + 2 \alpha(z) (1 - \alpha(z)) \text{cov}(\langle \theta_h' \rangle, \langle T'_{s_0} \rangle) \end{aligned} \quad (\text{A20})$$

$$\begin{aligned} \sigma_{q(z)}^2 &= (\gamma T_{\text{deep}} \beta \alpha(z))^2 \sigma_{T_{s_0}}^2 + (1 - \beta \alpha(z))^2 \sigma_{q_h}^2 \\ &+ 2 \gamma T_{\text{deep}} \beta \alpha(z) (1 - \beta \alpha(z)) \text{cov}(\langle q_h' \rangle, \langle T'_{s_0} \rangle), \end{aligned} \quad (\text{A21})$$

$$\sigma_{H(z)}^2 = \sigma_{\langle H_h \rangle}^2 \left( \frac{z - z_i}{h - z_i} \right)^2, \quad (\text{A22})$$

$$\sigma_{\lambda E(z)}^2 = \sigma_{\langle \lambda E_h \rangle}^2 \left( \frac{z - z_i}{h - z_i} \right)^2. \quad (\text{A23})$$

We also have

$$\text{cov}(\langle T'_{s_0} \rangle, \widetilde{B}_n) = \frac{\text{cov}(\widetilde{B}_0, \widetilde{B}_n)}{4_s ST_{\text{deep}}^3 + \frac{\rho C_p}{r_a^c (1-\alpha(z_1))} + \frac{\rho \lambda \beta \gamma T_{\text{deep}}}{r_a^c (1-\beta \alpha(z_1))}}, \quad (\text{A24})$$

$$\text{cov}(\langle \theta_h' \rangle, \widetilde{B}_n) = - \frac{\alpha(z_1)}{1 - \alpha(z_1)} \text{cov}(\langle T'_{s_0} \rangle, \widetilde{B}_n), \quad (\text{A25})$$

$$\text{cov}(\langle q_h' \rangle, \widetilde{B}_n) = - \frac{\beta \alpha(z_1) \gamma T_{\text{deep}}}{1 - \beta \alpha(z_1)} \text{cov}(\langle T'_{s_0} \rangle, \widetilde{B}_n). \quad (\text{A26})$$

## A2. Stochastic Harmonic Solution

[81] The harmonic solution of the stochastic problem and its derivation are, in essence, equivalent to the deterministic solution [Gentine *et al.*, 2010], except that the Fourier transform of the BB replaces that of the incoming radiation forcing at the land surface. Even though the time derivative of a stochastic process is ill defined, the partial differential equations in the soil and in the ABL are well defined. They are diffusion (heat) equations with no poles in the domain of interest and stochasticity only at the boundary. Specifically, we use the heat Kernel (Green's function) with stochastic forcing (Brownian bridge). The soil and ABL partial differential equations forced by a stochastic boundary noise become stochastic partial differential equations. Time derivatives are undefined for such problems. However, the projection on the Fourier basis is justified because of the pathwise convergence. The Fourier harmonics of the perturbed surface variables can be written

$$\begin{aligned} \widetilde{G}'(\omega_n, z = 0) &= \frac{1}{1 + 4 \epsilon_s ST_{\text{deep}}^3 \Delta(\omega_n) + \rho \Delta(\omega_n) \left( \frac{C_p}{r_a^c + \rho \Sigma(\omega_n)} + \frac{\lambda \beta \gamma T_{\text{deep}}}{r_a^c + \rho \beta \Sigma(\omega_n)} \right)} \widetilde{B}(\omega_n), \end{aligned} \quad (\text{A27})$$

$$\widetilde{\phi}_{\theta}'(\omega_n, z = h) = \frac{\Delta(\omega_n)}{(r_a^c + \rho \Sigma(\omega_n)) \left\{ 1 + 4 \epsilon_s ST_{\text{deep}}^3 \Delta(\omega_n) + \rho \Delta(\omega_n) \left( \frac{C_p}{r_a^c + \rho \Sigma(\omega_n)} + \frac{\lambda \beta \gamma T_{\text{deep}}}{r_a^c + \rho \beta \Sigma(\omega_n)} \right) \right\}} \widetilde{B}(\omega_n), \quad (\text{A28})$$

$$\widetilde{\phi}_q'(\omega_n, z = h) = \frac{\beta \gamma \langle T'_{s_0} \rangle \Delta(\omega_n)}{(r_a^c + \rho \beta \Sigma(\omega_n)) \left\{ 1 + 4 \epsilon_s ST_{\text{deep}}^3 \Delta(\omega_n) + \rho \Delta(\omega_n) \left( \frac{C_p}{r_a^c + \rho \Sigma(\omega_n)} + \frac{\lambda \beta \gamma T_{\text{deep}}}{r_a^c + \rho \beta \Sigma(\omega_n)} \right) \right\}} \widetilde{B}(\omega_n), \quad (\text{A29})$$

$$\begin{aligned} \tilde{T}'_s(\omega_n, z=0) &= \frac{1}{1/\Delta(\omega_n) + 4\epsilon_s ST_{\text{deep}}^3 + \rho \left( \frac{C_p}{r_a^c + \rho\Sigma(\omega_n)} + \frac{\lambda\beta\gamma T_{\text{deep}}}{r_a^c + \rho\beta\Sigma(\omega_n)} \right)} \tilde{B}(\omega_n), \end{aligned} \quad (\text{A30})$$

$$\tilde{\theta}'(\omega_n, z=h) = \frac{\rho\Sigma(\omega_n)}{(r_a^c + \rho\Sigma(\omega_n)) \left\{ 1/\Delta(\omega_n) + 4\epsilon_s ST_{\text{deep}}^3 + \rho \left( \frac{C_p}{r_a^c + \rho\Sigma(\omega_n)} + \frac{\lambda\beta\gamma T_{\text{deep}}}{r_a^c + \rho\beta\Sigma(\omega_n)} \right) \right\}} \tilde{B}(\omega_n), \quad (\text{A31})$$

$$\tilde{q}'(\omega_n, z=h) = \frac{\beta\gamma \langle T_{s_0} \rangle \rho\Sigma(\omega_n)}{(r_a^c + \rho\beta\Sigma(\omega_n)) \left\{ 1/\Delta(\omega_n) + 4\epsilon_s ST_{\text{deep}}^3 + \rho \left( \frac{C_p}{r_a^c + \rho\Sigma(\omega_n)} + \frac{\lambda\beta\gamma T_{\text{deep}}}{r_a^c + \rho\beta\Sigma(\omega_n)} \right) \right\}} \tilde{B}(\omega_n). \quad (\text{A32})$$

The stochastic solutions in the ABL are expressed as a function of land-surface values:

$$\tilde{\phi}'_b(\omega_n, z) = \tilde{\phi}'_b(\omega_n, z=h) \sqrt{\frac{z-d}{h-d} \frac{H_1^1(x_i)H_1^2(x) - H_1^2(x_i)H_1^1(x)}{H_1^1(x_i)H_1^2(x_h) - H_1^2(x_i)H_1^1(x_h)}}, \quad (\text{A33})$$

$$\tilde{\phi}'_q(\omega_n, z) = \tilde{\phi}'_q(\omega_n, z=h) \sqrt{\frac{z-d}{h-d} \frac{H_1^1(x_i)H_1^2(x) - H_1^2(x_i)H_1^1(x)}{H_1^1(x_i)H_1^2(x_h) - H_1^2(x_i)H_1^1(x_h)}}, \quad (\text{A34})$$

$$\begin{aligned} \tilde{\theta}'(\omega_n, z) &= \tilde{\phi}'_b(\omega_n, z=h) \frac{1+j}{\sqrt{2\omega_n Ku_*^0 (h-d)}} \\ &\quad \cdot \frac{H_1^1(x_i)H_0^2(x) - H_1^2(x_i)H_0^1(x)}{H_1^1(x_i)H_1^2(x_h) - H_1^2(x_i)H_1^1(x_h)}, \end{aligned} \quad (\text{A35})$$

$$\begin{aligned} \tilde{q}'(\omega_n, z) &= \tilde{\phi}'_q(\omega_n, z=h) \frac{1+j}{\sqrt{2\omega_n Ku_*^0 (h-d)}} \\ &\quad \cdot \frac{H_1^1(x_i)H_0^2(x) - H_1^2(x_i)H_0^1(x)}{H_1^1(x_i)H_1^2(x_h) - H_1^2(x_i)H_1^1(x_h)}, \end{aligned} \quad (\text{A36})$$

and similarly, in the soil,

$$\tilde{G}'(\omega_n, z) = \tilde{G}'(\omega_n, z=0) \exp\left( (1+j) \sqrt{\frac{\omega_n}{2K_s}} z \right), \quad (\text{A37})$$

$$\tilde{T}'_s(\omega_n, z) = \tilde{G}'(\omega_n, z=0) \frac{1-j}{C_s} \sqrt{\frac{1}{2\omega_n K_s}} \exp\left( (1+j) \sqrt{\frac{\omega_n}{2K_s}} z \right). \quad (\text{A38})$$

The stochastic problem is thus entirely solved with the specifications of the steady state and harmonic solutions. The dependence on height or depth can be investigated, as well as any time dependency. Because of the linearity of the soil-ABL model, all random variables are normally distributed and all stochastic processes are Gaussian; therefore,

the specification of the covariance function alone is sufficient to entirely determine the distribution of the variables of interest. Moreover, the BB and measurement at height  $z_1$  are centered therefore all variables are also centered (zero-mean processes and variables).

## Appendix B: Electrical Circuit Analogy

[82] In this appendix an electrical circuit analogue of the coupled soil-vegetation-atmosphere system is developed that responds to the fluctuations in land-surface temperature  $T_{s_0}$ . The problem is solved using Mathworks© Simulink (see Figure B1). The soil and atmospheric continuum is modeled using impedances between discrete temperatures. The current in the electrical circuit represents the heat fluxes within the system in watts per square meter, and the potentials represent the temperature away from the mean daily soil equilibrium value  $T_{\text{deep}}$ , that is,  $T_s - T_{\text{deep}}$  or  $\theta - T_{\text{deep}}$ . In the remainder of this appendix we use the notation  $T_s$  ( $\theta$ ) instead of  $T_s - T_{\text{deep}}$  ( $\theta - T_{\text{deep}}$ ) for a matter of simplicity.

[83] We first calculate the equivalent resistances between the potentials. In the near-surface atmosphere we know that the surface sensible heat flux  $H_h$  remains relatively constant with height and is given by

$$H_h = \frac{\rho C_p}{r_a^c} (T_{s_0} - \theta_h), \quad (\text{B1})$$

so that the resistance in the near-surface boundary layer can be defined as  $r_a^{c'} = r_a^c / \rho C_p$ . In the surface layer, the changes in sensible heat flux are small compared to those in the temperature. A surface-layer resistance can consequently be defined between height  $h$  and  $z_{\text{SL}}$  (top of the surface layer) using the conservation of the flux:

$$r_a^{\text{SL}} = 1/\rho C_p Ku_* \ln\left( \frac{z_{\text{SL}} - d}{h - d} \right). \quad (\text{B2})$$

In the mixed layer the sensible heat flux is quasi-linear, and we can use this property to express the difference between the temperature on top of the ABL and the temperature on top of the surface layer:

$$H(z_{\text{SL}}) = \frac{\rho C_p Ku_*}{1 - \frac{z_i - d}{z_i - z_{\text{SL}}} \ln\left( \frac{z_i - d}{z_{\text{SL}} - d} \right)} (\theta_{\text{SL}} - \theta_{\text{ML}}). \quad (\text{B3})$$

[84] Similarly, in the soil we define resistances between the soil temperatures, except that in the near surface a

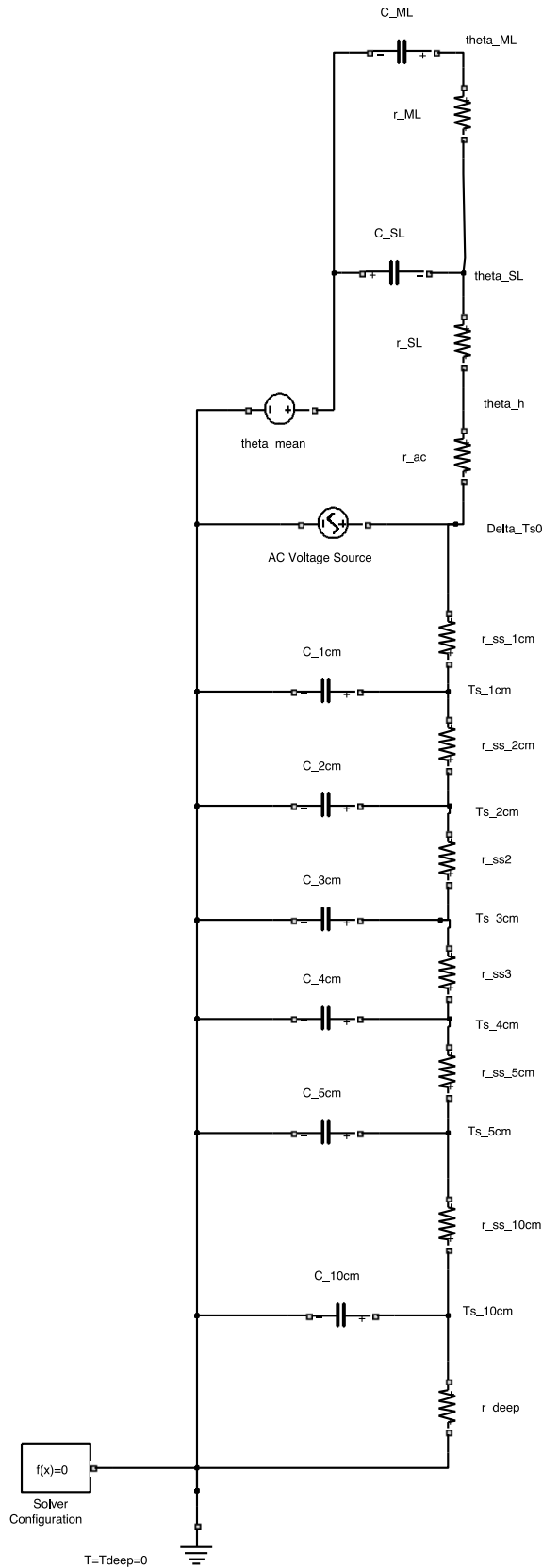


**Figure B1.** Schematic electrical circuit representation of the soil-vegetation-atmosphere coupling and its response to land-surface temperature changes.

thinner resolution is used, with intervals of 1 cm in the first 5 cm. The resistances in the five first centimeters are given by  $r_s^s = z_{1\text{cm}}/K_s$  between each 1 cm layer. Similarly, a resistance can be defined between  $T_{s_{10\text{cm}}}$  and  $T_{\text{deep}}$ , assuming that the latter temperature is fixed. Therefore, the deep resistance is given by  $r_s^{\text{deep}} = (z_{\text{deep}} - z_{10\text{cm}})/(\lambda_s C_s)$ . The first-order derivative changes of the temperatures are modeled with capacitances, as seen in Figure B1, for the sake of legibility. In all simulations the land-surface temperature is assumed to have a 10 K amplitude at any frequency.

[85] The asymptotic behavior of this circuit gives insights into the model response, at high versus low frequencies, to the land-surface temperature forcing. At high frequencies the capacitance are equivalent to a pure wire (short circuit). Therefore, at very high frequencies the temperature at 1 cm in the soil is directly linked to the reference potential. The gradient at the surface (i.e., the soil heat flux) is consequently very sharp because it is driven by the gradient between the land-surface temperature (10 K in this example) and the zero reference. In the atmosphere the resistances are larger, and there exists an offset of the mean temperature (written as  $\theta_{\text{mean}}$ ). Thus, the gradient (or sensible heat flux) is much lower than the one in the soil. In addition, since the surface resistance is varying in  $1/(\lambda_s C_s)$  and the capacitance is varying in  $C_s$ , the soil heat capacity is the main factor controlling the response of soil heat flux at high frequencies since an increase of  $C_s$  both decreases the surface resistance (increasing the surface gradients) and limits the soil temperature rise.

[86] At very low frequencies the capacitances are equivalent to an open circuit; therefore, the changes in land-surface temperature propagate in both media, the soil and the ABL. This results in a much-reduced soil heat flux because the soil temperature surface gradients are further diminished.

## Notation

### Main Text

- $\beta$  Beta parameterization of latent heat flux 0.6 as introduced by *Deardorff* [1978].
- $\epsilon_s$  Emissivity of the surface, 0.99.
- $\gamma$  Psychrometric constant, 0.577215.
- $\gamma_T \frac{\partial q^*}{\partial T}(T, P_0)$  ( $\text{kg kg}^{-1} \text{K}^{-1}$ ).
- $\lambda$  Specific latent heat of vaporization ( $2.45 \times 10^6 \text{ J kg}^{-1}$ ).
- $\lambda_s$  Soil thermal conductivity ( $\text{W m}^{-1} \text{K}^{-1}$ ).
- $\lambda E(z)$  Latent heat flux at height  $z$  ( $\text{W m}^{-2}$ ).
- $\lambda E_h$  Latent heat flux at the land surface, i.e., at canopy height  $h$  ( $\text{W m}^{-2}$ ).
- $\omega$  Angular frequency of the harmonic ( $\text{rad s}^{-1}$ ).
- $\Omega$  Rotation rate of the Earth ( $\text{rad s}^{-1}$ ).
- $\omega_0$  Fundamental angular frequency  $2\pi/T_{\text{day}}$  ( $7.29 \times 10^{-5} \text{ rad s}^{-1}$ ).
- $\phi$  Latitude (Marrakech) ( $31^\circ 37' \text{N}$ ).
- $\phi_\theta$  Turbulent heat flux of potential temperature ( $\text{K m s}^{-1}$ ).
- $\phi_\theta = w'\theta' = \frac{H}{\rho C_p}$ .
- $\phi_q$  Turbulent flux of specific humidity ( $\text{kg kg}^{-1} \text{m s}^{-1}$ ).
- $\phi_q = w'q' = \frac{\lambda E}{\rho \lambda}$ .
- $\rho$  Density of the air ( $1.2 \text{ kg m}^{-3}$ ).

- $\sigma$  Volatility of the Brownian bridge such that  $\sigma\sqrt{T}/2 = 25 \text{ W m}^{-2}$  (standard deviation at noon) ( $\text{W m}^{-2} \text{ s}^{-1/2}$ ).
- $\Sigma$  Stefan-Boltzmann's constant ( $5.67 \times 10^{-8} \text{ W m}^{-2} \text{ K}^{-4}$ ).
- $\theta$  Potential temperature in the boundary layer (K).
- $B_{T_{\text{day}}}$  Brownian bridge at the land surface ( $\text{W m}^{-2}$ ).
- $\widehat{B}_n$  nth Fourier harmonic of the Brownian bridge ( $\text{W m}^{-2}$ ).
- $C_s$  Soil heat capacity ( $1.42 \times 10^6 \text{ J m}^{-3} \text{ K}^{-1}$ ).
- $C_p$  Specific heat of air at constant pressure ( $1012 \text{ J kg}^{-1} \text{ K}^{-1}$ ).
- $d$  Displacement height (m).
- $f$  Coriolis parameter.
- $G(z)$  Ground heat flux at depth  $z$  ( $\text{W m}^{-2}$ ).
- $G_0$  Ground heat flux at the land surface ( $\text{W m}^{-2}$ ).
- $h$  Vegetation height (0.45 m).
- $H(z)$  Sensible heat flux at height  $z$  ( $\text{W m}^{-2}$ ).
- $H_h$  Sensible heat flux at the land surface, i.e., at canopy height  $h$  ( $\text{W m}^{-2}$ ).
- $K_s$  Soil thermal diffusivity ( $2.5 \times 10^{-7} \text{ m}^2 \text{ s}^{-1}$ ).
- $k$  von Karman constant (0.4).
- $I_{\downarrow}$  Incoming (shortwave and longwave) radiation at the land surface ( $\text{W m}^{-2}$ ).
- $L_{\uparrow}$  Outgoing longwave radiation at the land surface ( $\text{W m}^{-2}$ ).
- $P_0$  Surface pressure ( $1.013 \times 10^6 \text{ Pa}$ ).
- $q$  Specific humidity ( $\text{kg kg}^{-1}$ ).
- $q^*$  Specific humidity at saturation ( $\text{kg kg}^{-1}$ ).
- $r_a^c$  Canopy aerodynamic resistance ( $90 \text{ s m}^{-1}$ ).
- $S_{\downarrow}$  Incoming shortwave radiation at the land surface ( $\text{W m}^{-2}$ ).
- $R_n$  Net radiation at the land surface ( $\text{W m}^{-2}$ ).
- $T_{\text{day}}$  Time period of the whole experiment (86400 s).
- $T_s$  Soil temperature (K).
- $T_{s_0}$  Land-surface temperature (K).
- $T_{s_{10\text{cm}}}$  Soil temperature at 10 cm (K).
- $T_{\text{day}}$  Duration of a day (86400 s).
- $T_{\text{deep}}$  Soil temperature at infinite depth (K).
- $u_*$  Friction velocity ( $0.1 \text{ m s}^{-1}$ ).
- $W_T$  Brownian motion at the land surface ( $\text{W m}^{-2}$ ).
- $z$  Height/depth variable (m).
- $z_i$  Boundary-layer height (m).
- $z_1$  Height of mean-daily value specification (m).
- $z_{\text{meas}}$  Screen-level measurement height (2 m).

## Appendix B

- $C_{\text{ML}}$  Mixed-layer potential temperature capacitance ( $3.05 \times 10^5 \text{ J m}^{-2} \text{ K}$ ).
- $C_{\text{SL}}$  Surface-layer potential temperature capacitance ( $1.81 \times 10^3 \text{ J m}^{-2} \text{ K}$ ).
- $C_h$  Potential temperature capacitance at height  $h$  ( $85.15 \text{ J m}^{-2} \text{ K}$ ).
- $C_s^s$  Soil surface heat capacitance (1 cm layer) ( $2 \times 10^4 \text{ J m}^{-2} \text{ K}$ ).
- $C_s^{10\text{cm}}$  Soil heat capacitance between 5 cm and 10 cm ( $10^5 \text{ J m}^{-2} \text{ K}$ ).
- $r_a^{\text{ML}}$  Mixed-layer air resistance ( $0.0879 \text{ K W}^{-1}$ ).
- $r_a^{\text{SL}}$  Surface-layer air resistance ( $0.0663 \text{ K W}^{-1}$ ).
- $r_a^c$  Surface air resistance ( $0.0769 \text{ K W}^{-1}$ ).

- $r_s^s$  Soil surface resistance (1 cm layer) ( $0.0250 \text{ K W}^{-1}$ ).
- $r_s^{10\text{cm}}$  Soil resistance between 5 cm and 10 cm ( $0.125 \text{ K W}^{-1}$ ).
- $r_s^{\text{deep}}$  Deep soil surface resistance (10 cm to 1 m) ( $2.2500 \text{ K W}^{-1}$ ).

[87] **Acknowledgments.** This work was carried out with support from the grant titled "Direct Assimilation of Remotely Sensed and Surface Temperature for the estimation of Surface Fluxes" from the National Aeronautics and Space Administration to the Massachusetts Institute of Technology. The authors thank the SudMed project team for providing the experimental data set from the region of Marrakech, Morocco. The authors would like to thank Emmanuel Schertzer in the Mathematics Department at Columbia University for valuable comments on the approach used in this work. We would like to thank two anonymous reviewers for their valuable comments on the manuscript.

## References

- Baudena, M., F. D'Andrea, and A. Provenzale (2008), A model for soil-vegetation-atmosphere interactions in water-limited ecosystems, *Water Resour. Res.*, **44**, W12429, doi:10.1029/2008WR007172.
- Brubaker, K., and D. Entekhabi (1995), An analytic approach to modeling land atmosphere interaction: 1. Construct and equilibrium behavior, *Water Resour. Res.*, **31**, 619–632.
- Callies, U., A. Rhodin, and D. Eppel (1998), A case study on variational soil moisture analysis from atmospheric observations, *J. Hydrol.*, **213**, 95–108.
- Chehbouni, A., et al. (2008), An integrated modelling and remote sensing approach for hydrological study in arid and semi-arid regions: The SUDMED Programme, *Int. J. Remote Sens.*, **29**, 5161–5181.
- Deardorff, J. (1978), Efficient prediction of ground surface temperature and moisture, with inclusion of a layer of vegetation, *J. Geophys. Res.*, **83**, 1889–1903.
- Deardorff, J. (1979), Prediction of convective mixed-layer entrainment for realistic capping inversion structure, *J. Atmos. Sci.*, **36**, 424–436.
- Dehevels, P. (2007), A Karhunen–Loève expansion for a mean-centered Brownian bridge, *Stat. Probab. Lett.*, **77**, 1190–1200.
- Dickinson, R. (1988), The force–restore model for surface temperatures and its generalizations, *J. Clim.*, **1**, 1086–1097.
- Duchemin, B., et al. (2006), Monitoring wheat phenology and irrigation in central morocco: On the use of relationships between evapotranspiration, crops coefficients, leaf area index and remotely-sensed vegetation indices, *Agric. Water Manage.*, **79**, 1–27, doi:10.1016/j.agwat.2005.02.013.
- Gentine, P., D. Entekhabi, A. Chehbouni, G. Boulet, and B. Duchemin (2007), Analysis of evaporative fraction diurnal behaviour, *Agric. For. Meteorol.*, **143**, 13–29.
- Gentine, P., D. Entekhabi, and J. Polcher (2010), Spectral behaviour of a coupled land-surface and boundary-layer system, *Boundary Layer Meteorol.*, **134**, 157–180.
- Hess, R. (2001), Assimilation of screen level observations by variational soil moisture analysis, *Meteorol. Atmos. Phys.*, **77**, 145–154.
- Hu, Z., and S. Islam (1995), Prediction of ground surface temperature and soil moisture content by the force-restore method, *Water Resour. Res.*, **31**, 2531–2539.
- Huang, H.-Y., and S. A. Margulis (2010), Evaluation of a fully coupled large-eddy simulation-land surface model and its diagnosis of land-atmosphere feedbacks, *Water Resour. Res.*, **46**, W06512, doi:10.1029/2009WR008232.
- Jacobs, A., B. Heusinkveld, and S. Berkowicz (2000), Force-restore technique for ground surface temperature and moisture content in a dry desert system, *Water Resour. Res.*, **36**, 1261–1268.
- Kim, C., and D. Entekhabi (1998), Feedbacks in the land-surface and mixed-layer energy budgets, *Boundary Layer Meteorol.*, **88**, 1–21.
- Kimura, F., and Y. Shimizu (1994), Estimation of sensible and latent heat fluxes from soil surface temperature using a linear air land heat-transfer model, *J. Appl. Meteorol.*, **33**, 477–489.
- Lettau, H. (1951), Theory of surface temperature and heat-transfer oscillations near level ground surface, *Eos Trans. AGU*, **32**(2), 189.
- Manqian, M., and J. Jinjun (1993), A coupled model on land-atmosphere interactions—Simulating the characteristics of the pbl over heterogeneous surface, *Boundary Layer Meteorol.*, **66**, 247–264.
- Margulis, S., and D. Entekhabi (2001), A coupled land surface-boundary layer model and its adjoint, *J. Hydrometeorol.*, **2**, 274–296.

- Mihailovic, D., G. Kallos, I. Arsenic, B. Lalic, B. Rajkovic, and A. Papadopoulos (1999), Sensitivity of soil surface temperature in a force-restore equation to heat fluxes and deep soil temperature, *Int. J. Climatol.*, *19*, 1617–1632.
- Noilhan, J., and J. Mahfouf (1996), The ISBA land surface parameterisation scheme, *Global Planet. Change*, *13*, 145–159.
- Santanello, J., M. Friedl, and W. Kustas (2005), An empirical investigation of convective planetary boundary layer evolution and its relationship with the land surface, *J. Appl. Meteorol.*, *44*, 917–932.
- Santanello, J. A., M. A. Friedl, and M. B. Ek (2007), Convective planetary boundary layer interactions with the land surface at diurnal time scales: Diagnostics and feedbacks, *J. Hydrometeorol.*, *8*, 1082–1097, doi:10.1175/JHM614.1.
- Savijarvi, H. (1992), On surface temperature and moisture prediction in atmospheric models, *Beitr. Phys. Atmos.*, *65*(4), 281–292.
- Tennekes, H. (1973), A model for the dynamics of the inversion above a convective boundary layer, *J. Atmos. Sci.*, *30*, 558–567.
- Troen, I., and L. Mahrt (1986), A simple model of the atmospheric boundary layer; sensitivity to surface evaporation, *Boundary Layer Meteorol.*, *37*, 129–148.
- Wang, Z., and L. Mysak (2000), A simple coupled atmosphere-ocean-sea ice-land surface model for climate and paleoclimate studies, *J. Clim.*, *13*, 1150–1172.
- Van de Wiel, B. V., A. Moene, O. Hartogensis, H. D. Bruin, and A. Holtslag (2003), Intermittent turbulence in the stable boundary layer over land. Part III: A classification for observations during CASES-99, *J. Atmos. Sci.*, *60*, 2509–2522.
- Zeng, N., and J. Neelin (1999), A land-atmosphere interaction theory for the tropical deforestation problem, *J. Clim.*, *12*, 857–872.
- 
- D. Entekhabi, Ralph M. Parsons Laboratory, Department of Civil and Environmental Engineering, Massachusetts Institute of Technology, 77 Massachusetts Ave., Cambridge, MA 02139, USA. (darae@mit.edu)
- P. Gentine, Department of Applied Physics and Applied Mathematics, Columbia University, 500 W 120th St., New York, NY 10027, USA. (pg2328@columbia.edu)
- J. Polcher, Laboratoire de Météorologie Dynamique du CNRS, IPSL, Tour 45-55, 3ème étage, 4 Pl. Jussieu, F-75005 Paris, France. (jan.polcher@lmd.jussieu.fr)